2-2022

Primary deposition and early diagenetic effects on the high saturation accumulation of gas hydrate in a silt dominated reservoir in the Gulf of Mexico

Joel E. Johnson
University of New Hampshire - Main Campus, joel.johnson@unh.edu

Douglas MacLeod
University of New Hampshire

Stephen C. Phillips
U.S. Geological Survey

Marcie Purkey Phillips
University of Texas

David L. Divins
University of New Hampshire, David.Divins@unh.edu

Recommended Citation

Johnson, J.E., MacLeod, D.R., Phillips, S.C., Purkey Phillips, M., Divins, D.L., 2022. Primary deposition and early diagenetic effects on the high saturation accumulation of gas hydrate in a silt dominated reservoir in the Gulf of Mexico. Marine Geology, Volume 444, Feb., 106718, https://doi.org/10.1016/j.margeo.2021.106718

Marine Geology 444 (2022) 106718

Contents lists available at ScienceDirect

Marine Geology

journal homepage: www.elsevier.com/locate/margo

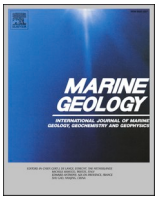

Primary deposition and early diagenetic effects on the high saturation accumulation of gas hydrate in a silt dominated reservoir in the Gulf of Mexico

Joel E. Johnson [a,*], Douglas R. MacLeod [a], Stephen C. Phillips [b,c], Marcie Purkey Phillips [c], David L. Divins [d]

[a] University of New Hampshire, Department of Earth Sciences, 56 College Road Durham, NH 03824, United States of America
[b] U.S. Geological Survey, 384 Woods Hole Road, Woods Hole, MA 02543, United States of America
[c] University of Texas at Austin, Institute for Geophysics, Jackson School of Geosciences, 10100 Burnet Road (R2200), Austin, TX 78758, United States of America
[d] University of New Hampshire, Institute for the Study of Earth, Oceans and Space, 8 College Road Durham, NH 03824, United States of America

ARTICLE INFO

Editor: Adina Paytan

Keywords:
Methane hydrate
Channel levee
Turbidites
Anaerobic oxidation of methane

ABSTRACT

On continental margins, high saturation gas hydrate systems (>60% pore volume) are common in canyon and channel environments within the gas hydrate stability zone, where reservoirs are dominated by coarse-grained, high porosity sand deposits. Recent studies, including the results presented here, suggest that rapidly deposited, silt-dominated channel-levee environments can also host high saturation gas hydrate accumulations. Here we present several sedimentological data sets, including sediment composition, biostratigraphic age from calcareous nannofossils, grain size, total organic carbon (TOC), C/N elemental ratio, δ^{13}C-TOC, $CaCO_3$, total sulfur (TS), and δ^{34}S-TS from sediments collected with pressure cores from a gas hydrate rich, turbidite channel-levee system in the Gulf of Mexico during the 2017 UT-GOM2-1 Hydrate Pressure Coring Expedition. Our results indicate the reservoir is composed of three main lithofacies, which have distinct sediment grain size distributions (type A-silty clay to clayey silt, type B-clayey silt, and type C-sandy silt to silty sand) that are characteristic of variable turbidity current energy regimes within a Pleistocene (< 0.91 Ma) channel-levee environment. We document that the TOC in the sediments of the reservoir is terrestrial in origin and contained within the fine fraction of each lithofacies, while the $CaCO_3$ fraction is composed of primarily reworked grains, including Cretaceous calcareous nannofossils, and part of the detrital load. The lack of biogenic grains within the finest grained sediment intervals throughout the reservoir suggests interevent hemipelagic sediments are not preserved, resulting in a reservoir sequence of silt dominated, stacked turbidites. We observe two zones of enhanced TS at the top and bottom of the reservoir that correspond with enriched bulk sediment δ^{34}S, indicating stalled or slowly advancing paleo-sulfate-methane transition zone (SMTZ) positions likely driven by relative decreases in sedimentation rate. Despite these two diagenetic zones, the low abundance of diagenetic precipitates throughout the reservoir allowed the primary porosity to remain largely intact, thus better preserving primary porosity for subsequent pore-filling gas hydrate. In canyon, channel, and levee environments, early diagenesis may be regulated via sedimentation rates, where high rates result in rapid progression through the SMTZ and minimal diagenetic mineralization and low rates result in the stalling of the SMTZ, enhancing diagenetic mineralization. Here, we observed some enhanced pyritization to implicate potential sedimentation rate changes, but not enough to consume primary porosity, resulting in a high saturation gas hydrate reservoir. These results emphasize the important implications of sedimentary processes, sedimentation rates, and early diagenesis on the distribution of gas hydrate in marine sediments along continental margins.

* Corresponding author.
E-mail address: joel.johnson@unh.edu (J.E. Johnson).

https://doi.org/10.1016/j.margeo.2021.106718
Received 2 November 2021; Received in revised form 23 December 2021; Accepted 23 December 2021
Available online 29 December 2021

1. Introduction

Marine gas hydrates form and accumulate within the gas hydrate stability zone (GHSZ) in continental margin sediments throughout the global oceans. The gas trapped within marine gas hydrate is most commonly methane (Kvenvolden, 1993; Milkov, 2005) and thus it is referred to as methane hydrate. Although methane hydrate is nearly ubiquitous within the marine GHSZ, its concentration is highly variable (e.g., Trehu et al., 2004). In the marine environment, methane hydrate forms within both sediment and fracture porosity under conditions of low salinity, cold bottom water temperatures (~4 °C), water depths >500 m (Ruppel and Kessler, 2017) and methane concentrations at or above methane solubility (Xu and Ruppel, 1999). In marine sediments, the geothermal gradient restricts methane hydrate formation to the upper few hundred meters of the sediment column (Ruppel and Kessler, 2017), often in unconsolidated/unlithified sediments.

Sediments of large grain size within the GHSZ, such as turbidite sands and silts, offer high porosity with large pore throats that enhance permeability and the potential to transport and store large quantities of free gas and gas hydrate (Boswell and Collett, 2006). Constraining the amount and distribution of gas hydrate in marine continental margins requires scientific sampling/coring and geophysical logging through ocean drilling (e.g., Trehu et al., 2004; Yamamoto, 2015; Collett et al., 2014, 2019; Flemings et al., 2020). Scientific ocean drilling and sampling have enabled detailed study of the physical, chemical, and microbiological characteristics and dynamics of gas hydrate systems and have improved our understanding of gas hydrate systems throughout the global oceans. Given the large spatial extent of global continental margins, however, these studies remain limited. Continued study of marine gas hydrates is valuable as they represent a potentially enormous, yet ephemeral reservoir of carbon on Earth (Dickens, 2003; Archer et al., 2009; Ruppel and Kessler, 2017) and they may be an economically viable, cleaner, transitional hydrocarbon resource in the future (Boswell, 2009; Boswell and Collett, 2011; Boswell et al., 2020) as society moves toward truly renewable energy sources. Coarse-grained gas hydrate reservoirs may also be a potential target for coupled methane production and carbon dioxide sequestration (Koh et al., 2016; Boswell et al., 2017; Darnell et al., 2017).

In addition to the thermodynamic and chemical controls on gas hydrate stability, gas hydrate also requires accessible pore space and/or fracture space in order to accumulate in marine sediments. In the marine environment, accessible primary porosity and permeability is found in coarse-grained, sand-rich deepwater deposits (Torres et al., 2008; Yoneda et al., 2017; Fang et al., 2020). In contrast, clay-dominated deposits have low sediment permeability, restricting gas hydrate accumulation to secondary fractures (Cook and Goldberg, 2008; Cook et al., 2014). High primary porosity and permeability in coarse-grained stratigraphic intervals is driven by coarse particle size accumulation on the continental shelf and subsequent transport of sand and silt sized particles to deepwater environments via turbidity currents and other sediment gravity flows. Submarine canyon and channel-levee systems on the continental slope and rise coincide with the GHSZ and coarse-grained sediments can accumulate here due to variations in sediment routing down the slope that are often controlled by tectonic or diapiric deformation. Turbidite sand deposits hosting gas hydrate in continental slope environments off the coasts of India (Collett et al., 2019), Japan (Yamamoto, 2015; Fujii et al., 2015), and the United States (Riedel et al., 2010; Torres et al., 2008; Boswell et al., 2012a) have been the focus of recent gas hydrate investigations. Channel deposits are typically coarser than levee deposits, owing to a higher depositional energy within the confined, main channel, and therefore have greater pore space capacity to store gas hydrate under equivalently favorable gas hydrate stability conditions. However, silty levee deposits can also have significant gas hydrate storage capacity, especially if the deposits are stacked into multi-event stratigraphic intervals (e.g. Meazell et al., 2020; Phillips et al., 2020; this study) and have high enough intrinsic permeability (Fang et al., 2020).

In this paper we present several sedimentological data sets including sediment composition, biostratigraphic age, grain size, TOC, C/N, δ^{13}C-TOC, $CaCO_3$, TS, and δ^{34}S-TS content and isotopic signatures that collectively explain, from a depositional and early diagenetic perspective, why gas hydrate accumulates within a silt-dominated methane hydrate-bearing reservoir in the northern Gulf of Mexico basin. Sediments for our analyses were sampled from pressure cores collected during the UT-GOM2-1 Hydrate Pressure Coring Expedition in 2017 (Flemings et al., 2018) and recovered from the levee of a Pleistocene-age submarine channel in the Green Canyon 955 (GC 955) lease block in the Gulf of Mexico. The data presented here document that (1) this methane hydrate-bearing reservoir is composed of three distinct, grain size-defined, lithofacies that are consistent with deposition via turbidity currents, (2) the predominance of silt throughout the reservoir is driven by high energy overbank turbidity currents deposited frequently in time, (3) the detrital fraction in the sediments is dominated by reworked carbonate lithic fragments and Cretaceous calcareous nannofossils, (4) TOC is present throughout the reservoir, but sorted in the fine fraction within each lithofacies, and (5) early diagenetic processes associated with anaerobic oxidation of methane were dominant in two intervals within the reservoir, rather than throughout the reservoir, likely due to the variable sedimentation rates associated with deposition of these sediments and their relatively fast migration through the SMTZ, which minimized secondary precipitates (e.g. AOM produced Fe-sulfides and authigenic carbonates) and maintained primary porosity for later methane hydrate formation.

2. Geologic setting

The northern Gulf of Mexico basin is characterized by thick accumulations (~15–20 km) of terrigenous and marine sediments that were originally deposited over the Jurassic Louann Salt deposits (Watkins et al., 1978; Peel et al., 1995). Bathymetry in the northern Gulf of Mexico basin is significantly influenced by migrating salt structures in the subsurface (Jackson and Talbot, 1986; Peel et al., 1995). Seismic reflection data have identified salt sills and diapirs that directly influence prominent bathymetric features throughout the Gulf of Mexico (e.g. Ewing and Ewing, 1962) including the Sigsbee escarpment, which has a relief of up to 900 m caused by horizontally migrating salt (Amery, 1969; Worrall and Snelson, 1989). Landward of the Sigsbee escarpment, the seafloor is pocked with salt-withdrawal basins (e.g., Prather et al., 1998) created by salt diapirs that breached the seafloor and subsequently dissolved. Migrating salt causes deformation (folding and fracturing) of adjacent seafloor sediments, which creates migration pathways and structural traps for hydrocarbons that have been exploited by the oil and gas industry in the Gulf of Mexico. Seismic reflection imaging and BSR (bottom simulating reflector) mapping documents salt tectonics drives deformation throughout the Gulf of Mexico and largely controls gas migration pathways and subsequent gas hydrate system development and accumulation (Shedd et al., 2012; Portnov et al., 2020a; Santra et al., 2020).

Gas hydrate has been widely inferred from seismic reflection profiles in the northern Gulf of Mexico (Shipley et al., 1979; Kou et al., 2007; Shedd et al., 2012; Hillman et al., 2017; Madof, 2018; Portnov et al., 2019; Portnov et al., 2020b) and inferred at multiple locations during the 2009 Gulf of Mexico Joint Industry Project Leg II (JIP II) logging-while-drilling (LWD) expedition (Boswell et al., 2012a) and from petroleum industry well logs (Majumdar et al., 2016, 2017). These hydrate occurrences collectively represent a substantial volume of gas hydrate on the order of trillions of m^3 of natural gas (Milkov and Sassen, 2001; Frye, 2008; Majumdar and Cook, 2018). JIP II confirmed the presence of high saturation methane hydrate hosted within coarser grained (sand and silt) reservoirs in several locations throughout the Gulf of Mexico, including GC 955 (Boswell et al., 2012b). Prior to the UT-GOM2-1 expedition, gas hydrates in the Gulf of Mexico had only been sampled

from near-seafloor sediments (Ruppel et al., 2005; Winters et al., 2007), seep environments (Brooks et al., 1984; Davidson et al., 1986; MacDonald et al., 1994; Sassen et al., 1999), or as low-saturation hydrate from scientific drilling cores (Pflaum et al., 1986; Kastner et al., 2008). Collectively, all of the results to date document that methane hydrate saturation in Gulf of Mexico sediments ranges from a few percent to >90% saturation, with the coarser, sand and silt-rich stratigraphic intervals containing the greatest saturations (e.g., Phillips et al., 2020).

3. Site characteristics: Green Canyon block 955

3.1. Physical setting

Our study area is located in the GC 955 lease block at a water depth of ~2000 m along the basinward margin of the Sigsbee escarpment at the mouth of Green Canyon in the northern Gulf of Mexico (Fig. 1). GC 955 hosts a series of paleo channel-levee complexes intersected by faults (McConnell, 2000; Hutchinson et al., 2009; Boswell, 2009; Haines et al., 2017; Santra et al., 2020). The JIP II expedition identified a high-resistivity, high-velocity, and low-natural gamma radiation interval using LWD data between 415 and 440 mbsf at GC 955 H001 indicating

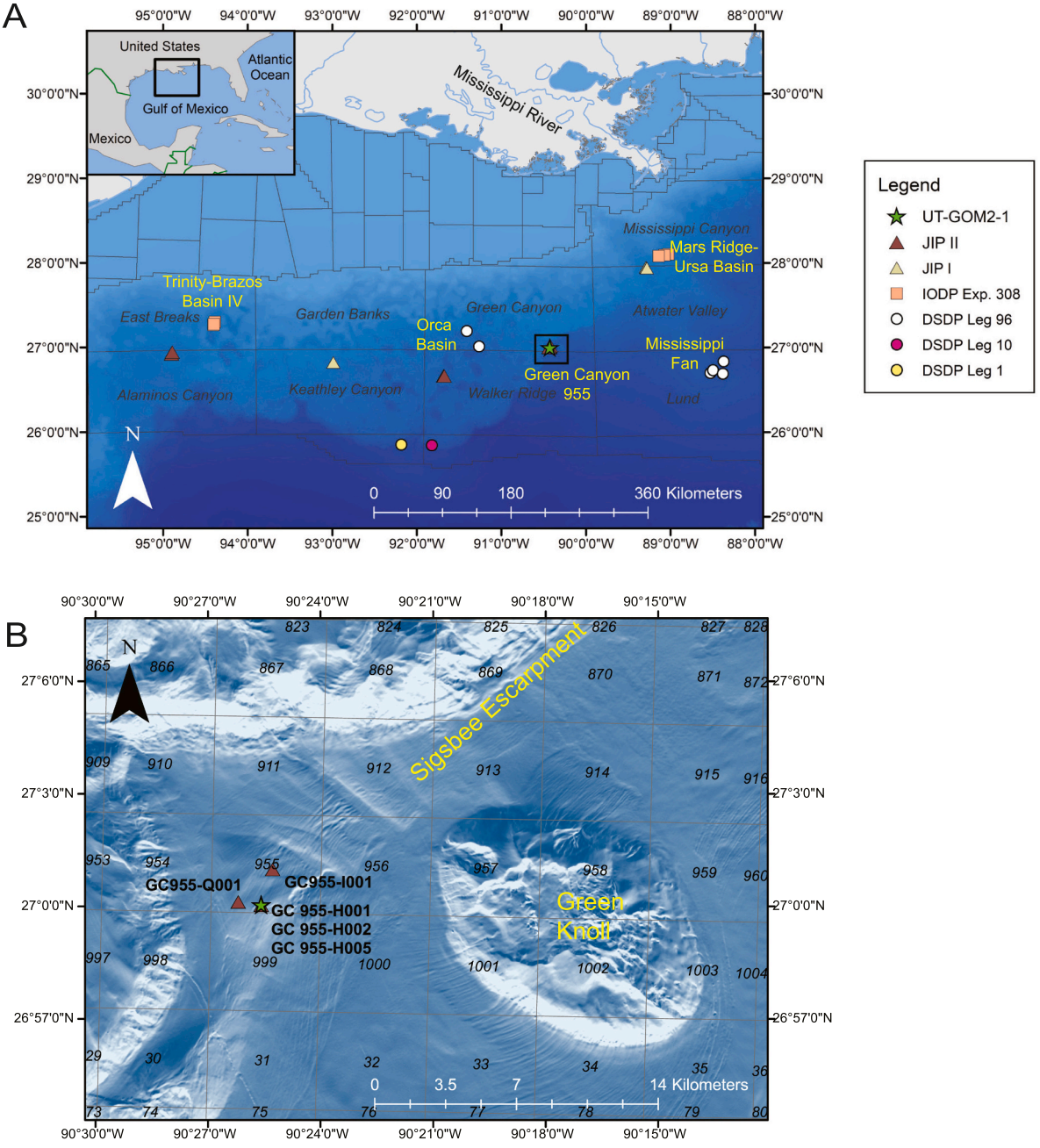

Fig. 1. (A) Location of study area in the Green Canyon 955 lease block in the Gulf of Mexico, 265 km south-south-west of Port Fourchon, LA. Existing JIP (Joint Industry Project), IODP and DSDP boreholes discussed in the text also shown. (B) The UT-GOM2-1 holes H002 and H005 are located at the GC 955 H001 site at the foot of the Sigsbee Escarpment at a water depth of approximately 2000 m. Bathymetry data from the Bureau of Ocean Energy Management Northern Gulf of Mexico Deepwater Bathymetry Grid (https://www.boem.gov/Gulf-of-Mexico-Deepwater-Bathymetry/); Kramer and Shedd (2017). (For interpretation of the references to color in this figure legend, the reader is referred to the web version of this article.)

the presence of a high methane hydrate saturation, coarse-grained reservoir (Boswell et al., 2012a). Fig. 1 shows the location of holes drilled in GC 955 during the JIP II expedition. Two of the three holes drilled in GC 955 during the JIP II expedition encountered methane hydrate, but full LWD data was only acquired for hole H001 due to drilling complications (Collett et al., 2012). Hole H001 was drilled in Fault Block H and was found to contain interbedded levee deposits with methane hydrate-bearing intervals occurring within the coarser stratigraphy of the GHSZ (Collett et al., 2012). The UT-GOM2-1 expedition pressure cores discussed here were recovered in 2017 and their collection was guided by the seismic and LWD data collected during JIP II.

3.2. GC 955 methane hydrate reservoir

The UT-GOM2-1 expedition in 2017 drilled two holes, H002 and H005, each within 30 m of hole H001 where methane hydrate was inferred in 2009 by JIP II (Flemings et al., 2018). The study location contains heterogeneous fractures filled with methane hydrate from ~186 to ~293 mbsf and a low average methane hydrate saturation (Boswell et al., 2012a). The primary methane hydrate reservoir, which has a methane hydrate saturation of up to 93% (Phillips et al., 2020), is at a depth of ~414 to ~450 mbsf based on data from the JIP II expedition. The gas is dominantly microbial methane (99.99%) with isotopic ratios that indicate methane was generated from primary CO_2 reduction methanogenesis (Moore et al., 2020, 2022). Gas hydrates at GC 955 contain trace levels of thermogenic components C2-C5 that increase near the base of the reservoir (Moore et al., 2022). Coring of H002 and H005 was designed to capture the entire primary methane hydrate reservoir and the bounding sedimentary units immediately above and below (Fig. 3).

Three distinct lithofacies (silty clay, clayey silt, and sandy silt) within the GC 955 methane hydrate reservoir were identified during the UT-

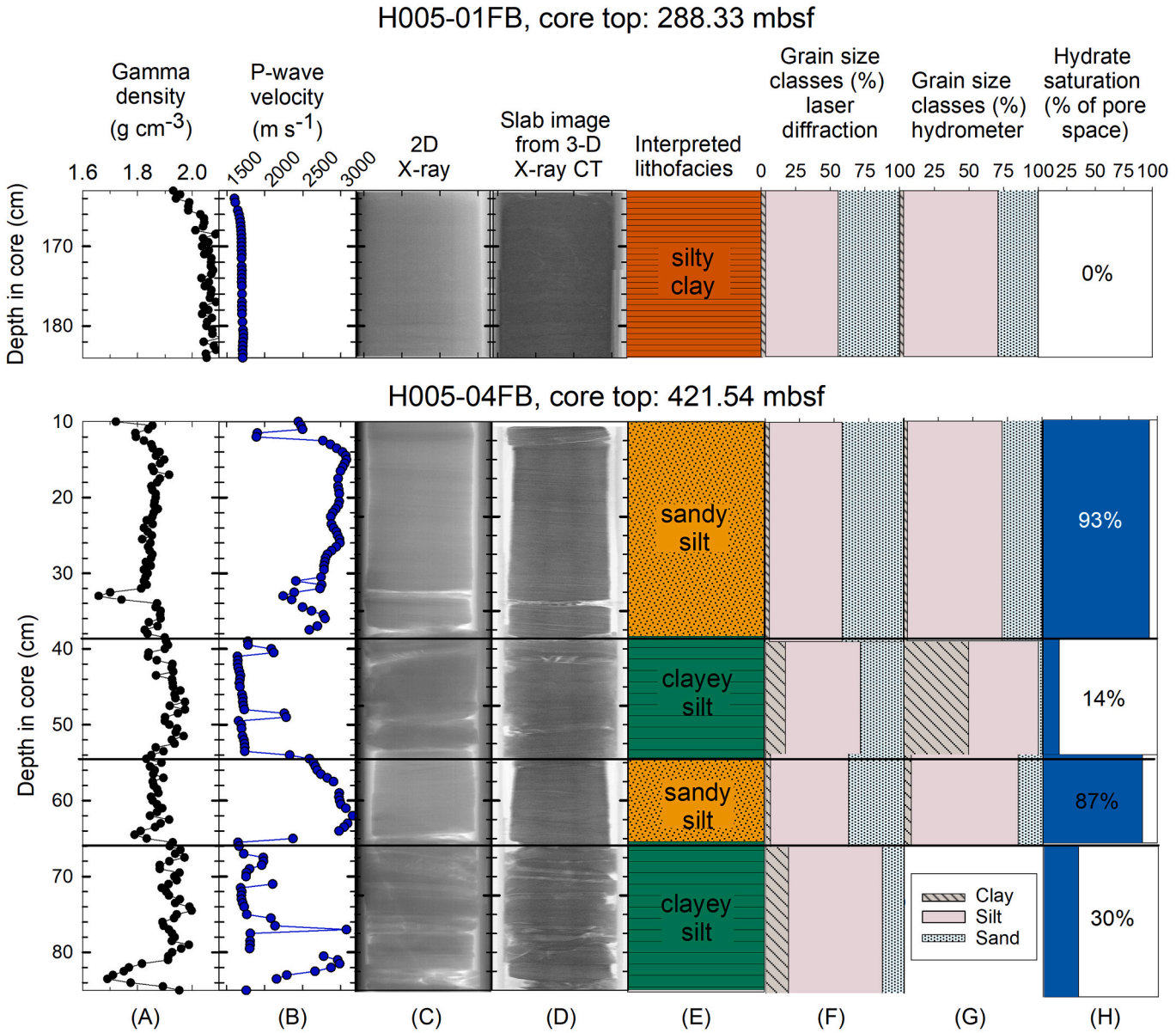

Fig. 2. Examples of the three main lithofacies observed during the UT-GOM2-1 expedition from pressure core scanning (A through D) (Flemings et al., 2018), quantitative degassing (H) (Phillips et al., 2020), and post-dissociation grain size analysis (F and G) (Meazell et al., 2020; Flemings et al., 2020). Methane hydrate is concentrated in the sandy silt, high P-wave velocity, lower density intervals, while the clayey silt and silty clay have low to zero hydrate saturation, low P-wave velocity and higher density. The methane hydrate-bearing sandy silt intervals are lighter in color on the X-ray scans and retain a narrower diameter within the core liner. (For interpretation of the references to color in this figure legend, the reader is referred to the web version of this article.)

GOM2-1 expedition based on initial pressure core scans of compressional wave (P-wave) velocity, gamma density, 2D X-ray, and 3D X-ray-computed tomography (CT), as well as post-dissociation grain size measurements (Flemings et al., 2020; Fig. 2). Initial grain size measurements from the reservoir were made with both laser diffraction and hydrometer measurements and indicated silty clay is the finest-grained lithofacies, with a median grain size of 1.4 μm (57% clay, 43% silt) and negligible methane hydrate saturation (Meazell et al., 2020; Phillips et al., 2020; Figs. 2 and 3). Sandy silt is the coarsest-grained lithofacies, with a median grain size ranging from 40 to 56 μm (18–40% sand, 60–77% silt; 2–5% clay) and the greatest methane hydrate saturations (79 to 93%) (Meazell et al., 2020; Phillips et al., 2020). Within the sandy silt, millimeter to centimeter scale rippled cross-laminations were commonly observed with X-ray-CT imaging of the pressure cores consistent with deposition by turbidity currents in a waning flow regime (e.g., Flemings et al., 2018; Meazell et al., 2020). The clayey silt lithofacies falls between sandy silt and silty clay, with a median grain size of 2.0 to 4.6 μm (1 to 7% sand, 49–60% silt, 38–49% clay and contains low/moderate methane hydrate saturation (Meazell et al., 2020; Phillips et al., 2020; Figs. 2 and 3) Within the main reservoir unit, sandy silt and clayey silt are interbedded on the scale of centimeters to up to 1 m (Meazell et al., 2020). Meazell et al. (2020) measured grain size using the hydrometer method and documents finer results compared to measurements by the laser diffraction method for the same lithofacies, especially with higher clay content. This observation has been noted in other studies (e.g. Di Stefano et al., 2010) and is attributed to non-spherical particles in the clay size fraction. Di Stefano et al. (2010) determined that there is no discernable difference between grain size measurements using a hydrometer and those made using laser diffraction systems on coarse, sand dominated grain sizes, but compared to the hydrometer method, laser particle size analyzers may underestimate the clay content in a sample.

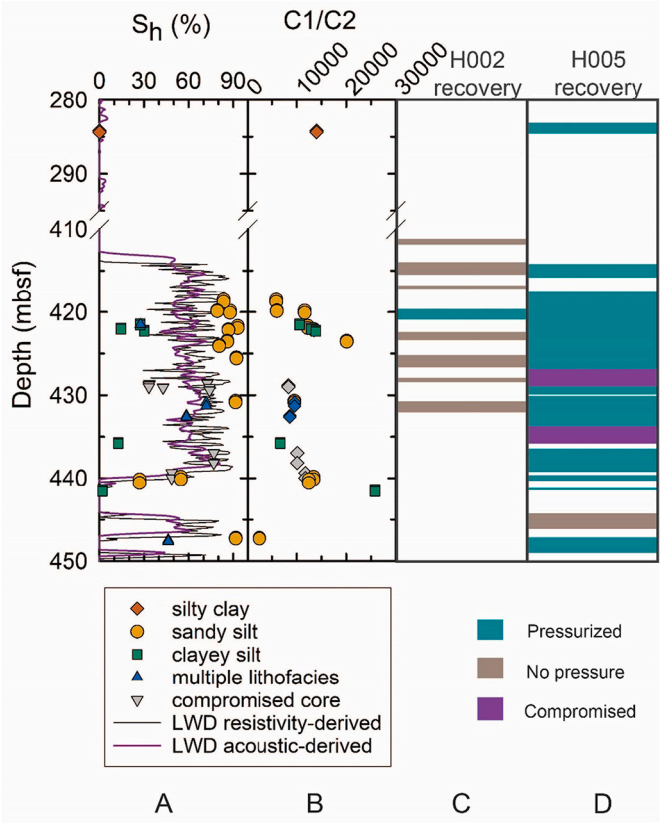

Fig. 3. A) Methane hydrate saturations at GC 955 from pressure core degassing during UT-GOM2-1 (symbols) (Phillips et al., 2020) and derived from LWD during JIP II (black and purple lines) (Lee and Collett, 2012). Grain size classes from laser diffraction particle size analysis (Flemings et al., 2020; Meazell et al., 2020). B) Methane/ethane ratio (C1/C2 from pressure core degassing). C) Pressure core recovery in Hole H002. D) Pressure core recovery in Hole H005. Multiple lithofacies sections contain multiple lithofacies within an individual degassing sample. Compromised cores briefly left the hydrate stability field during recovery or processing and may have experienced some dissociation prior to quantitative degassing. (For interpretation of the references to color in this figure legend, the reader is referred to the web version of this article.)

Building upon the initial UT-GOM2-1 expedition results, we completed detailed sediment core descriptions (Johnson and Divins, 2020) and core sampling and analyses that result in a rich data set of grain size (n = 46) (Johnson et al., 2020; MacLeod, 2020) and solid phase sediment geochemical measurements (n = 49) that we have synthesized and present in this paper.

4. Methods

4.1. Sample collection

All sediment samples used in this study were collected from pressure cores recovered during the 2017 UT-GOM2-1 expedition aboard the deepwater well intervention vessel Helix D/V Q4000. During the expedition a total of 21 pressure cores, each 3.05 m in length, were attempted between 2 holes drilled through a methane hydrate reservoir (Fig. 3). In hole H002, 1 of the 8 pressure cores attempted was recovered under pressure and there was a sediment recovery rate of 34% (Thomas et al., 2020). In hole H005, 12 of the 13 pressure cores attempted were recovered under pressure and there was a sediment recovery rate of 85% (Thomas et al., 2020). The majority of sediment samples analyzed in this study are from pressure cores that failed to retain pressure during recovery. These cores are stored at Ohio State University and were sampled during sediment core description in 2018 (Johnson and Divins, 2020). All samples labeled as “bagged” are from core sections with limited recovery that were removed from their core liners and stored in sealed plastic bags prior to sampling for various sediment analyses. Additional sediments were derived from pressure cores that were quantitatively degassed after recovery.

4.2. Sediment composition

Visual core descriptions (VCDs) are based on macroscopic and microscopic sediment type, sedimentary structures, and drilling disturbance. Visual core descriptions were completed on the subset of cores stored at Ohio State University and are summarized and available in Johnson and Divins (2020). Sediment composition data were determined from smear slide microscopic descriptions and are included in the above core descriptions and previously in the UT-GOM2-1 Expedition Report (Flemings et al., 2018) and discussed in Meazell et al. (2020). In this paper we present a brief summary of these results to provide context for our other measurements and importantly to document the carbonate components of the bulk sediment composition.

4.3. Sediment grain size

To characterize the sediment grain size in holes H002 and H005 at GC 955, we used a Malvern Mastersizer 2000 Laser Particle Size Analyzer with a Hydro 2000G wet dispersion unit at the University of New Hampshire (UNH). The Malvern Mastersizer 2000 measures particles ranging in diameter from 0.2 μm to 2000 μm. Malvern Mastersizer 2000 software (version 5.60) was used for all analyses. Optimal software settings (see Johnson et al., 2020) were determined empirically and are consistent with Sperazza et al. (2004). In total, we measured 51 sediment samples and the complete data set, initially presented and discussed in MacLeod (2020), is available as a data report (Johnson et al., 2020). Bulk sediments sampled for grain size (1 cm^3) were contained within 1 cm thick stratigraphic intervals, avoiding major lithologic or

grain size bed boundaries. This is one important advantage of laser diffraction compared with measurement of grain size by hydrometer, which in the Gulf of Mexico required a much larger sample size (35–70 g; Meazell et al., 2020). Our sampling strategy focused on characterizing the range of particle size distributions in these cores, within the context of the three lithofacies identified during X-ray CT and P-wave velocity scanning (e.g. Meazell et al., 2020) and split core description (Johnson and Divins, 2020).

Bulk sediment and total organic carbon-digested (TOC-free) sediment fractions were measured for most of the grain size samples (n = 46), while the remaining samples (n = 5) only had sufficient material to make TOC-free measurements (MacLeod, 2020; Johnson et al., 2020). Replicate samples (n = 23) of bulk and TOC-free sediments were also measured and show good agreement (MacLeod, 2020; Johnson et al., 2020). In addition, we measured a natural beach sand (Wallis Beach, NH Sand), and a synthetic Malvern 15–150 μm glass bead standard as check standards (MacLeod, 2020; Johnson et al., 2020) at the beginning and end of each day to ensure consistent instrument performance. The majority of the sediment samples analyzed for grain size in this study (n = 34) are from pressure cores that failed to retain pressure during recovery (see Thomas et al., 2020). These cores are stored at Ohio State University and were split and sampled during sediment core description in 2018. An additional 17 sediment samples from successful pressure cores were shipped to the UNH Sedimentology Lab for grain size analysis after being quantitatively degassed during shipboard and dockside operations or at the University of Texas at Austin Pressure Core Center (Phillips et al., 2020).

For the majority (46 of 51) of the grain size samples analyzed at the University of New Hampshire we measured both the bulk grain size and the TOC-free grain size distributions to determine the relative amount of particulate organic carbon in the samples and in what grain size fraction it resides. For bulk sample preparation, about 2 cm^3 of sediment was added to 50 mL centrifuge tubes with a solution of sodium hexametaphosphate (5 g/L of $(NaPO_3)_6$) up to the 25 mL line. The sodium hexametaphosphate solution helps to prevent fine-grained sediment particles from aggregating together during analysis. The tubes were capped and agitated for 60 s on a vortex mixer then left overnight. The following day, samples were mixed again for 60 s on the vortex mixer immediately before being added to the dispersion unit on the UNH Malvern Mastersizer 2000 laser diffractometer. For TOC-free sample measurements, the organic carbon was removed from the samples via a multi-step hydrogen peroxide treatment, prior to the sodium hexametaphosphate addition. Small volumes of 30% hydrogen peroxide were added to each sample and flushed with DI water, centrifuged, and decanted between additions until a total of 30 mL of hydrogen peroxide had been added to each sample to ensure all organic carbon was digested.

We used three equations developed by Folk and Ward (1957) to quantify statistical parameters of the measured grain size distributions. These equations are based on grain size units of phi (Φ) as calculated by a logarithmic transformation $\Phi = -log_2(d)$ where d represents the grain size diameter in mm. The phi grain size scale is commonly used in sedimentology and larger values indicate smaller grain diameter. Fig. 4 shows the three equations used during data analysis and an explanation of the range of output parameters. The subscript on equation terms indicates the grain size percentile. For example, Φ_{84} represents roughly the middle of the finest third of the sample and Φ_{16} represents roughly the middle of the coarsest third of the grain size distribution.

4.4. Biostratigraphy

Calcareous nannofossil biostratigraphy was determined from 34 samples examined from the UT-GOM2-1 pressure cores – 22 samples from Hole H002, and 12 samples from H005. The biozonation applied to the age estimation is the Calcareous Nannofossil Plio-Pleistocene (CNPL) Zonation of Backman et al. (2012), which assigns Plio-Pleistocene biochronology to calcareous nannofossil assemblages from low to middle latitudes. This biozonation is further calibrated to the 2016 Geologic Time Scale of Ogg et al. (2016). Semi-quantitative evaluations were conducted on all samples to identify age-diagnostic species/assemblages and estimate geologic age. All samples contain significant amounts of Cretaceous nannofossils that suggest reworking of sediments. These specimens are not considered part of the microfossil assemblage when

Sorting (σ)		Skewness (Sk)		Kurtosis (K)	
$\sigma = \frac{\Phi_{84}-\Phi_{16}}{4} + \frac{\Phi_{95}-\Phi_5}{6.6}$		$Sk = \frac{\Phi_{16}+\Phi_{84}-2\Phi_{50}}{2(\Phi_{84}-\Phi_{16})} + \frac{\Phi_5+\Phi_{95}-2\Phi_{50}}{2(\Phi_{95}-\Phi_5)}$		$K = \frac{\Phi_{95}-\Phi_5}{2.44(\Phi_{75}-\Phi_{25})}$	
Very well sorted	<0.35	Very positive skewed	0.3 to 1.0	Very platykurtic	<0.67
Well sorted	0.35-0.50	Positive skewed	0.1 to 0.3	Platykurtic	0.67-0.9
Moderately well sorted	0.50-0.70	Symmetrical	0.1 to -0.1	Mesokurtic	0.90-1.11
Moderately sorted	0.70-1.00	Coarse skewed	-0.1 to -0.3	Leptokurtic	1.11-1.50
Poorly sorted	1.00-2.00	Very coarse skewed	-0.3 to -1.0	Very leptokurtic	1.50-3.00
Very poorly sorted	2.00-4.00			Extremely leptokurtic	>3.00
Extremely poorly sorted	>4.00				

Fig. 4. Sorting, skewness, and kurtosis equations used in this analysis were developed by Folk and Ward (1957) to summarize grain size distribution data. Sorting is a measure of the spread of the grain size distribution about the average, skewness is a measure of the asymmetry of the grain size distribution, and kurtosis is a measure of peakedness of the grain size distribution.

making biostratigraphic age estimations; instead, they are considered part of the detrital sediment. The full biostratigraphy data set is available as data report (Purkey Phillips, 2020). In this paper we present the sediment age model and discuss the implications of the reworked Cretaceous nannofossils.

4.5. Elemental C, TOC, C/N, $CaCO_3$ and $\delta\ ^{13}C_{TOC}$ analysis

Elemental measurements and stable carbon isotopes were measured at the stable isotope lab at the University of New Hampshire in Durham, NH, USA, using an Elementar Americas Pyrocube elemental analyzer coupled to a GeoVision isotope ratio mass spectrometer.

Bulk sediment total C (TC), total N (TN), and carbonate free total organic carbon (TOC) were measured. Prior to TOC analysis, inorganic carbon (IC) was dissolved using 6% sulfurous acid applied to weighed samples in amounts and steps optimized for carbonate-rich sediments (Phillips et al., 2011). For the GC 955 samples, a total of 780 uL of sulfurous acid was added to each 20 mg powdered, dry, sediment sample used for TOC analysis. $CaCO_3$ weight percents were calculated by multiplying the IC weight percents (IC = TC-TOC) by 8.33 to account for the non-carbon mass fraction. The calculated bulk $CaCO_3$ fraction represents biogenic, authigenic, and any detrital carbonate phases. In addition to instrument standards and blanks, *Elemental Microanalysis* soil standards B2180 and B2182 (www.microanalysis.co.uk) were analyzed as unknowns and used to assess analytical precision and accuracy. Average values of C agree within the uncertainty of the certified values. Repeatability error was established by analyzing replicate samples and calculating the standard deviation (see Supplementary Table S1).

For the stable isotope measurements, the ratio of sample analyses to in-house standards analyzed was less than 3:1 and the measurement uncertainty of the instrument as determined by repeated analyses of in-house QA/QC standards was ±0.20‰ (±1σ) for $\delta^{13}C$. The measured ^{13}C abundance values are reported relative to VPDB (Vienna Pee Dee Belemnite) based on a 4-point normalization using contemporaneously analyzed in-house standards and 3 additional in-house standards were analyzed as unknowns for QA/QC. Stable carbon isotopic values of in-house standards were quantified relative to VPDB on a scale normalized such that the $\delta^{13}C$ values of NBS 19 calcium carbonate and LSVEC lithium carbonate are +1.95‰ and − 46.6‰, respectively, using a multi-point normalization (7 points) and the following international reference materials and isotopic values: IAEA-CH-7 ($\delta^{13}C$-VPDB = −32.151‰), NBS22 ($\delta^{13}C$-VPDB = −30.03‰), USGS40 ($\delta^{13}C$-VPDB = −26.39‰), USGS42 ($\delta^{13}C$-VPDB = −21.28‰), USGS43 ($\delta^{13}C$-VPDB = −21.09‰), IAEA-CH-6 ($\delta^{13}C$-VPDB = −10.449‰), and USGS41 ($\delta^{13}C$-VPDB = +37.63‰).

4.6. Elemental S and $\delta^{34}S$ analysis

Total sulfur (TS) and $\delta^{34}S$-TS measurements were determined at the Center for Stable Isotope Biogeochemistry at the University of California at Berkeley, USA. Dry and ground samples were analyzed for sulfur content (% dry weight) and sulfur stable isotope ratio ($\delta^{34}S$ value) via elemental analyzer/continuous flow isotope ratio mass spectrometry using a Flash IRMS elemental analyzer (EA Isolink CN with ramped GC oven for triple NCS analysis) coupled with a Delta V Plus mass spectrometer (Thermo Fisher Scientific, Waltham, MA, USA). Stable isotope abundances are reported in ‰ notation relative to the VCDT (Vienna-Canyon Diablo Troilite) standard. The full analytical procedure is presented in Mambelli et al. (2016). The standard deviation for replicate measurements are shown in the Supplemental Table S1.

5. Results

5.1. Sediment composition

Core description and smear slide sediment compositions from sediments recovered in the pressure cores in holes H002 and H005 (Johnson and Divins, 2020) reveal the reservoir is composed of interbedded, sandy silt to silty clay turbidite facies (Flemings et al., 2018; Meazell et al., 2020). Smear slide mineralogy in the turbidites is dominated by quartz, multiple feldspars (microcline, plagioclase, and orthoclase), and lithic fragments, primarily detrital carbonates (Fig. 5), which is consistent with measurements of bulk sediment mineralogy from X-ray diffraction (XRD) (Meazell et al., 2020; Heber et al., 2020). This mineral assemblage as plotted on the QFL diagram (Fig. 5A) falls along a similar compositional trend as DSDP Leg 96 cores on the Mississippi Fan, and the average mineralogy from samples collected in the Mississippi and Rio Grande Rivers (Fig. 5A), which supply most of the lithogenic sediment flux to the Gulf of Mexico. It is notable, however, that the GC 955 H002 and H005 samples are more mineralogically immature (containing a larger fraction of lithics) than the Mississippi and Rio Grande River deposits, and most of the Mississippi Fan sediments. In addition, the lithic fraction of the GC 955 samples is dominated by carbonate lithics (Fig. 5B), which are mineralogically and texturally immature. These observations are consistent with rapid deposition during turbidity current deposition and/or an offshore source area for the lithics observed in the H002 and H005 cores.

5.2. Sediment age control and reworking

Calcareous nannofossil biostratigraphy was determined from 33 samples across the UT-GOM2-1 GC 955 reservoir, and one from the overlying hemipelagic sediments – 22 samples from Hole H002, and 12 samples from H005 (Purkey Phillips, 2020) and provides an age estimation for the reservoir section (Fig. 6). All samples examined from UT-GOM2-1 holes H002 and H005 are estimated to be between 0.43 Ma and 0.91 Ma based on biohorizons from both Backman et al. (2012) and Waterman et al. (2017). This estimated age range straddles the Calabrian and Ionian stage boundary of the late Middle Pleistocene (Backman et al., 2012; Ogg et al., 2016; Waterman et al., 2017). More specifically, all samples are estimated to be within the Calcareous Nannofossil Pleistocene (CNPL) Zone 10 as defined by the Biozonation of Miocene-Pleistocene calcareous nannofossils from low- to mid-latitudes (Backman et al., 2012). The CNPL Zone 10 is concurrent with the more widely known Calcareous Nannofossil Zone NN19 (Martini, 1971). Despite turbiditic influences on these samples, the microfossils are still reliable, age-diagnostic tools. Of the 34 samples examined for biostratigraphy, 14 contained age-diagnostic assemblages (Purkey Phillips, 2020). Of those 14 samples, 11 were silt dominated in texture, yet contained age-diagnostic assemblages that were relatively reliable based on good preservation and moderate abundance. Three samples were exceptional with grain sizes (silty clay) more conducive to primary microfossil preservation, particularly sample H005-1FB-3_163-184 cm at 284.18 mbsf - the uppermost sample of the interval – which was taken from the hemipelagic overburden above the hydrate reservoir and is described as a silty clay lithofacies. H005-1FB was initially the only core between both holes with this lithologic description (Flemings et al., 2020; Meazell et al., 2020). The other two samples with higher quality microfossil assemblages are H002-5CS-1_75-76 cm, 422.29 mbsf and H002-8CS-4_5-6 cm, 433.08 mbsf, both depths within the middle of the reservoir.

The overall biostratigraphic interpretation is strengthened by integrating the data from both holes (only 12 m apart); and integration is supported by the correlation of hydrate-bearing layers between holes H002 and H005 (Thomas et al. (2020), as well as hole H001 that was drilled in 2009 (Purkey Phillips, 2020). Core recovery was significantly more successful in hole H005 (85%) than in H002 (34%) (Thomas et al., 2020). Cored material included both hydrate-bearing pressure cores and conventionalized pressure cores. Biostratigraphy samples were collected from both types of cored material, including failed pressure cores. *In situ* microfossil assemblages were more robust in hole H002, but more age-diagnostic species were identified in hole H005, further supporting the

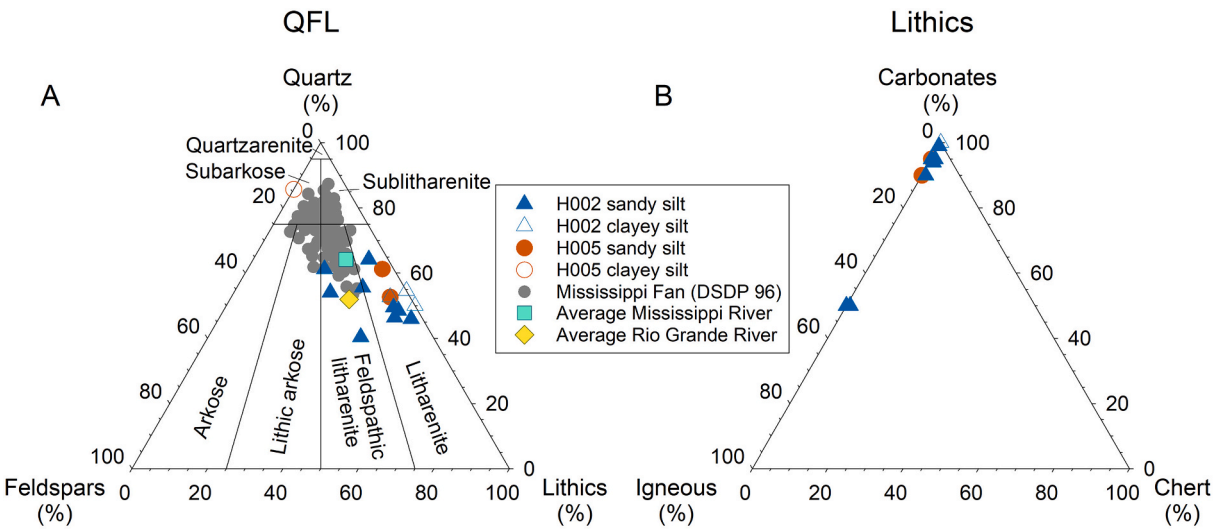

Fig. 5. (A) Summary QFL ternary plot of sediment compositions from DSDP Leg 96 (Thayer et al., 1986), Mississippi and Rio Grande River deposits (Potter, 1978), and UT-GOM2-1 sediments (this study). UT-GOM2-1 normalized % estimates of quartz, total feldspar, and total lithics grains were obtained from smear slide descriptions. (B) Lithic ternary plot for UT-GOM2-1 sediments; notice detrital carbonates with a small admixture of igneous lithics dominate the overall lithic fraction. (For interpretation of the references to color in this figure legend, the reader is referred to the web version of this article.)

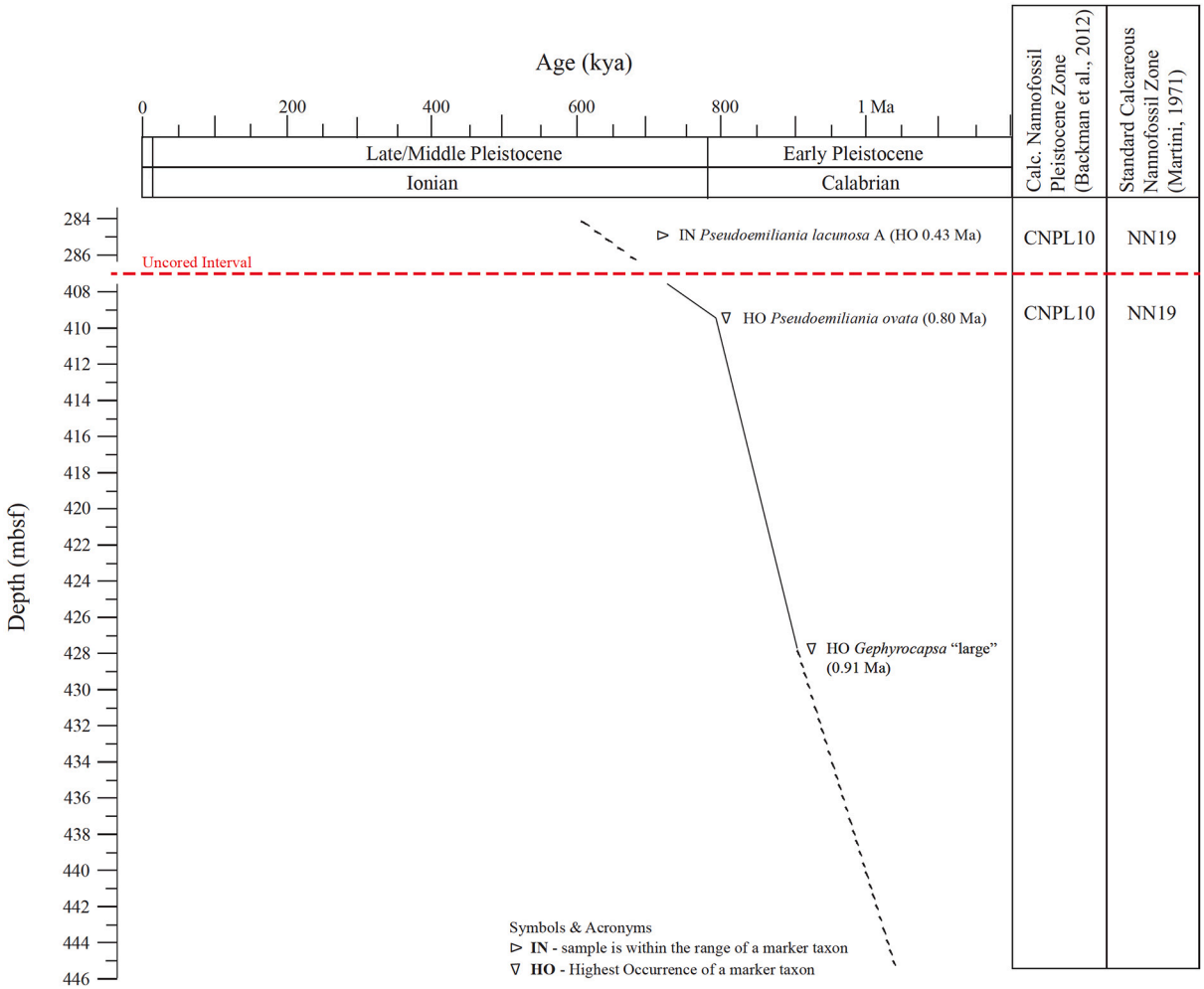

Fig. 6. A composite Age/Depth plot for Calcareous Nannofossils recovered in UT-GOM2-1 Holes H002 and H005. Calcareous nannofossil events are from both the Biostratigraphic Chart-Gulf Basin, USA produced by PaleoData Inc. Waterman et al. (2017) and the Pliocene/Pleistocene biozonation of Backman et al. (2012). The geologic timescale is that of Ogg et al. (2016). The complete calcareous nannofossil data set is available as a data report (Purkey Phillips, 2020).

value of data integration between holes.

In addition to the Pleistocene microfossil assemblage, a relatively abundant and diverse reworked Cretaceous nannofossil assemblage was observed in every sample, especially from within the reservoir lithofacies (Fig. 7). This reworked assemblage is preserved throughout the reservoir in the channel-levee lithology and represents part of the detrital sediment flux that was eroded and transported from the North American craton. High abundances of reworked calcareous nannofossils were observed in sediments of the Mississippi Fan and the Orca Basin recovered during Deep Sea Drilling Project Leg 96 (Constans and Parker, 1986). Further work from a core in the Orca Basin by Marchitto and Wei (1995) suggests that increases in reworked nannofossils in the Gulf of Mexico correspond to erosion driven by low stands and glacial meltwater pulses.

5.3. Sediment grain size

Grain size analysis of bulk sediment samples shows three distinct patterns of grain size distribution; A, B, and C, which are in order of increasing median grain size (Fig. 8). A total of 46 bulk sediment samples were analyzed including 13 A-type samples, 4 B-type samples, and 29C-type samples. Average median grain size, skewness, kurtosis, and sorting for each of the three distribution types are shown in Table 1. The textural name for each sample is classified from the percent sand, silt, and clay of each sample and plotted on the ternary textural classification diagram (Fig. 9). Individual grain size distribution plots for each sample and the data tables are archived in Johnson et al. (2020).

A-type grain size samples are poorly to very poorly sorted with grain size distributions that are approximately evenly split between clay and silt with very minimal sand (Fig. 8). The skewness of the A-type grain size distributions is approximately symmetrical, ranging from slightly positive to slightly negative. The kurtosis of the A-type grain size distributions is platykurtic, due to the broad grain size distribution and poor sorting. Several A-type samples display a secondary modal peak in their coarse fraction. In terms of their textural classification, A-type sediments range from clayey silt to silty clay (Fig. 9). B-type grain size samples are very poorly sorted and have distinctly bimodal grain size distributions (Fig. 8). The skewness of the B-type grain size distributions

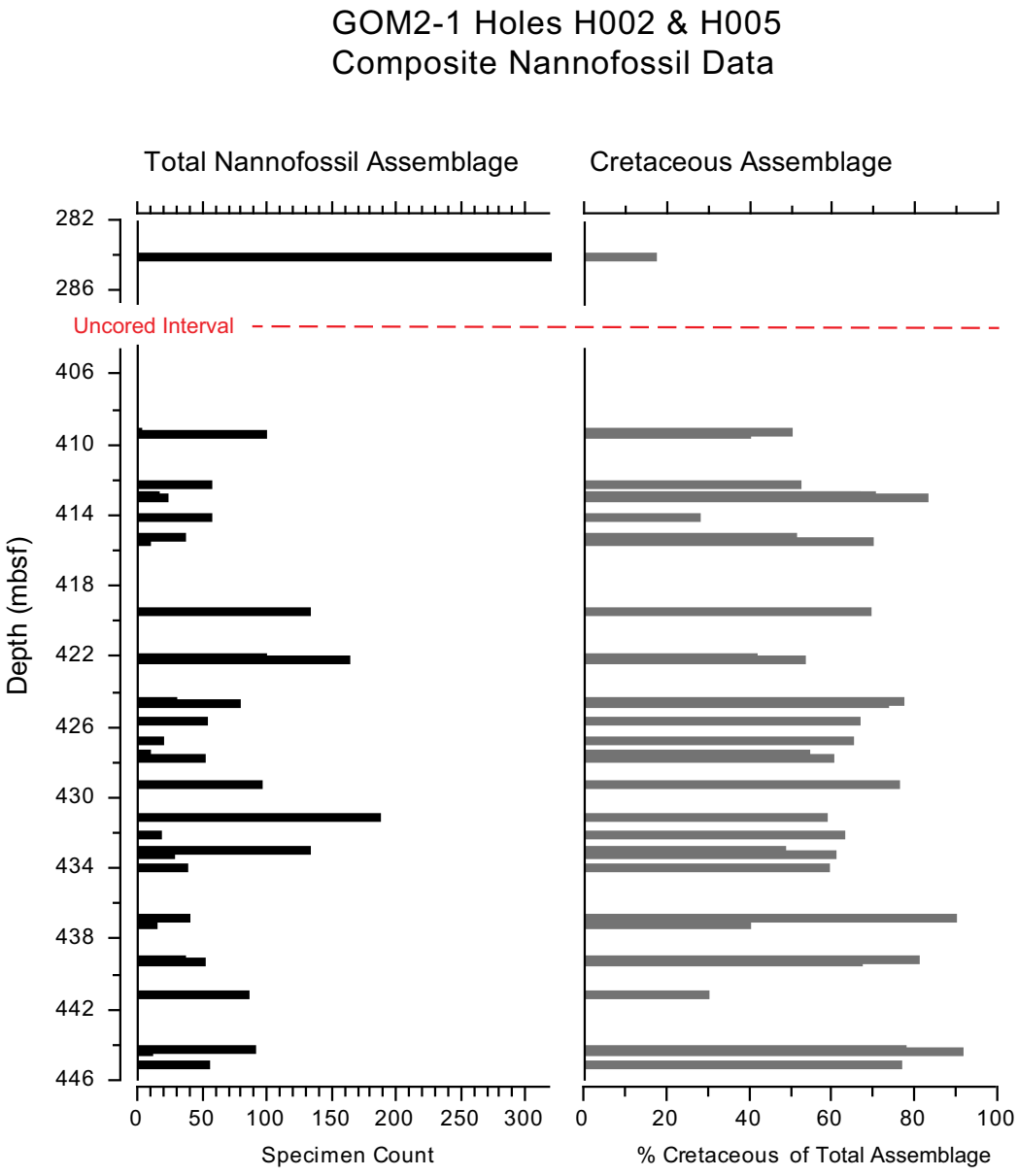

Fig. 7. Percent Cretaceous calcareous nannofossils relative to the total assemblage within the Early Pleistocene UT-GOM2-1 reservoir stratigraphy.

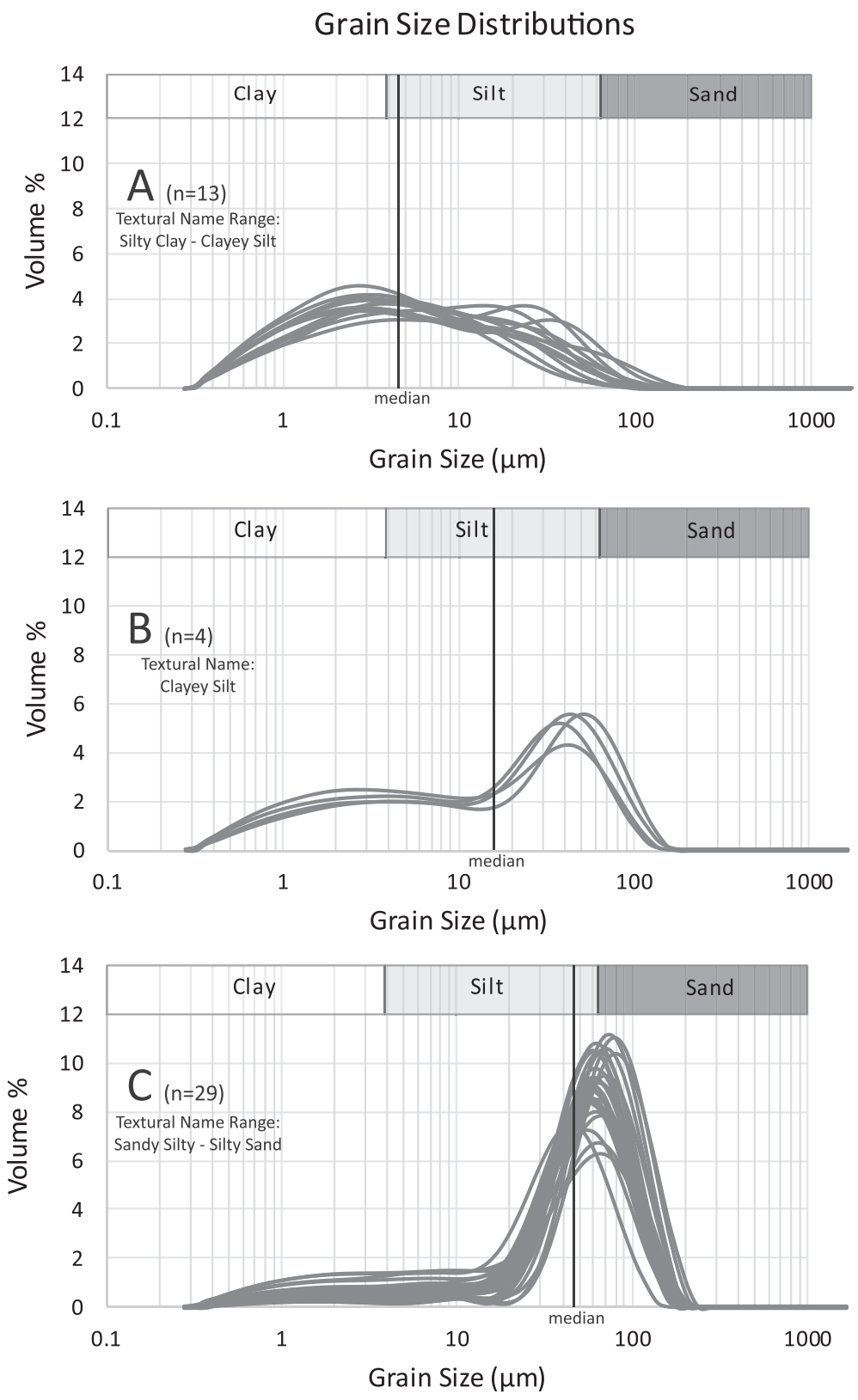

Fig. 8. Grain size distribution summary plots for the UT-GOM2-1 GC 955 reservoir. Bulk sediment grain size measurements reveal three dominant distributions, A, B, and C with increasing median grain size respectively. Grain size distribution statistics are shown in Table 1. Textural name ranges described in the text and in Fig. 9 are also shown.

Table 1
Average median grain size, skewness, kurtosis, and sorting of bulk grain size measurements, shown to the 95% confidence interval.

Bulk sample	Median (μm)	Skewness	Kurtosis	Sorting (σ)	n =
Type A	4.55 ± 0.63	-0.04 ± 0.03	0.86 ± 0.02	1.91 ± 0.08	13
Type B	17.15 ± 5.16	0.33 ± 0.10	0.76 ± 0.03	2.23 ± 0.05	4
Type C	48.21 ± 3.27	0.43 ± 0.03	1.68 ± 0.11	1.51 ± 0.13	29

is skewed very positive due to a secondary modal peak residing in the finer grain size fraction. The kurtosis of the B-type grain size distributions is platykurtic and is significantly influenced by the distinctly bimodal distribution. In terms of their textural classification, B-type sediments are all clayey silt (Fig. 9). C-type samples are poorly sorted and have grain size distributions with a strong unimodal peak at approximately the silt/sand grain size boundary, and fine-grained tails of varying significance (Fig. 8). The skewness of the C-type grain size distributions is very positively skewed due to the fine-grained tails. The kurtosis of the C-type grain size distributions is very leptokurtic despite the presence of significant fine-grained tails. In terms of their textural classification, C-type sediments are predominantly sandy silt, with some silty sand (Fig. 9).

Variation in the grain size distributions with depth in the reservoir is shown in the 3-D plot of Fig. 10. The presentation of grain size distributions and textural names in Figs. 8, 9, and 10 reveals the silt dominance of the reservoir and the persistent fine grain fractions (clay to fine silt) that are present within each distribution type (Fig. 8). Interbedded silt- and clay-dominated intervals within the reservoir reflect the high energy regime during turbidity current deposition and the lower energy regime characterized by waning turbidity current energy and/or hemipelagic settling between turbidity current events.

5.4. Sorting

Comparison between the sorting and median grain size of the sediment samples further supports the presence of three distinct grain size distribution types (Fig. 11). C-type samples have the largest range of sorting values due to the variable thickness of their fine-grained tails (e.g., Fig. 8). A-type samples are much less sorted compared to most C-type samples and are uniformly finer-grained. B-type samples appear to fall between A and C-type samples, likely representing a transitional distribution type, consistent with their distinct bimodal nature (Fig. 8).

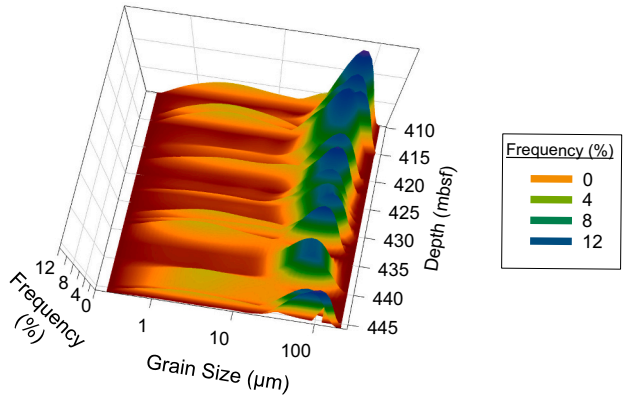

Fig. 10. Stacked bulk sediment grain size distributions (n = 46) throughout the UT-GOM2-1 GC 955 reservoir. Notice the strong silt/sand peak juxtaposed against the smaller but significant fine-grained particles present in all three lithofacies. (For interpretation of the references to color in this figure legend, the reader is referred to the web version of this article.)

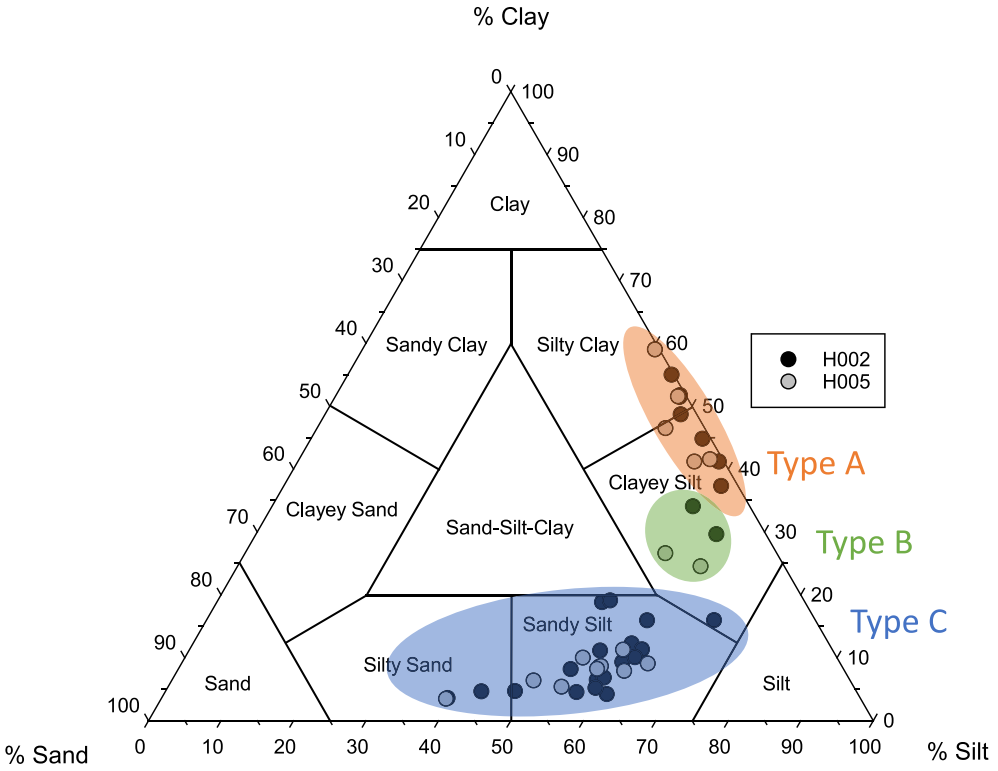

Fig. 9. Ternary textural classification for the UT-GOM2-1 GC 955 bulk sediment samples (n = 46) measured in this study. A, B, and C-type distributions as noted in the text and in Fig. 8. Sand, silt, and clay percentages were calculated using the Wentworth Grain Size scale (Wentworth, 1922), where sand is > 62.5 μm, clay is < 3.9 μm, and silt is between 62.5 and 3.9 μm. (For interpretation of the references to color in this figure, the reader is referred to the web version of this article.)

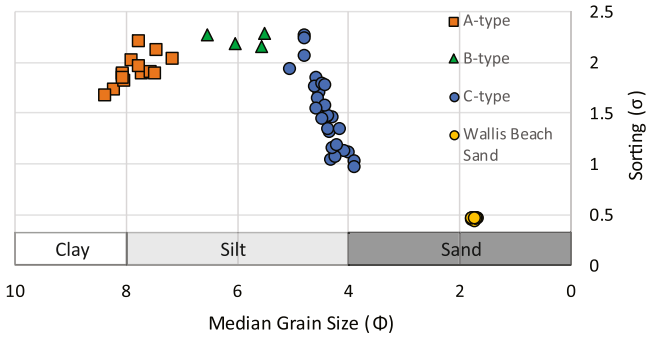

Fig. 11. Sorting and median grain size of bulk sediment A, B, and C-type grain size distributions. The Wallis Beach sand (New Hampshire, USA) is shown for reference as a well sorted, coarse-grained sample we use as a check standard. (For interpretation of the references to color in this figure legend, the reader is referred to the web version of this article.)

5.5. Organic carbon-free vs bulk grain size

Comparison between bulk and TOC-free measurements for each sample reveals numerous instances (28 out of 46) where grain size distributions shifted toward the coarser fraction after hydrogen peroxide treatment was used to remove organic carbon. In samples where grain size distributions have shifted after hydrogen peroxide treatment, the organic carbon predominantly resided within the fine grain size fraction as demonstrated by a relative loss in the finest material in all three distribution types (A, B, and C) (Fig. 12). The preferential volumetric loss of organic carbon in the fine fraction resulted in a relative increase of the coarser faction. Three examples of samples showing a loss of organic carbon in the fine fraction are shown in Fig. 12, one for each grain size distribution type (A, B, and C). A loss of organic carbon in the fine fraction is not exclusive to any of the three identified grain size distributions (A, B, or C-type). Figures showing the comparisons of all bulk and TOC-free measurements are shown in MacLeod (2020) and archived in Johnson et al. (2020). The remaining 18 samples, for which both bulk and TOC-free grain size distributions were measured, showed little-to-no change in their grain size distributions, irrespective of the three grain size distributions (A, B, and C-type) (MacLeod, 2020; Johnson et al., 2020). As suggested by MacLeod (2020), this could indicate either low TOC within many of these samples, extremely fine organic carbon trapped in nanopores on the face of sediment grains (e.g., Mayer, 1994) or organic matter distributed within the carbonate lithic fragments that is inaccessible to removal with hydrogen peroxide and/or too small for the laser particle size analyzer to measure.

5.6. Replicate grain size measurements

A total of 23 samples were randomly chosen for replicate grain size analysis including 15 TOC-free and 8 bulk samples. Additionally, the standard operating procedure we used on the Malvern Mastersizer laser particle size analyzer includes triplicate measurement of each sample aliquot to ensure consistent instrument performance. Replicate grain size measurements for Type A, B, and C distributions are nearly indistinguishable (MacLeod, 2020). In general, TOC-free replicate measurements performed slightly better than bulk replicate measurements, demonstrating the consistency of the hydrogen peroxide procedure used to remove organic carbon. These replicate measurements are shown in Johnson et al. (2020).

5.7. Bulk geochemistry

A total of 49 samples were analyzed separately for TC, TOC, TC, TN, TS, C/N, δ^{13}C-TOC, δ^{13}C-TC, and δ^{34}S-TS from both holes H002 and H005. The composite results from both holes H002 and H005 are shown in Figs. 13–16 and are discussed below. The data are presented in Supplementary Data Table S1.

5.7.1. TOC and $\delta^{13}C$ isotopes, C/N, and $CaCO_3$

The mean TOC throughout the sampled interval is 0.63 wt% ($1\sigma = 0.23$ wt%) and ranged from 0.19 to 1.02 wt%. The variation in the TOC content throughout reservoir (Fig. 13) is driven largely by the variation in the host sediment lithofacies of the levee depositional environment, but all lithofacies samples contain some measurable TOC. For samples with both TOC and grain size measurements, we note a strong relationship between grain size and TOC, where finer grained sediments contain greater TOC than coarser grained sediments (Fig. 14).

The origin of the TOC is determined by its TOC/TN and δ^{13}C-TOC isotopic signature. The mean atomic TOC/TN ratio is 20.7 and ranges from 9.1 to 34.8. The mean δ^{13}C-TOC is −25.43 per mil ($1\sigma = 0.55$) and ranges from −24.09 per mil to −26.65 per mil. The δ^{13}C-TOC is remarkably consistent throughout the reservoir (Fig. 14) and together with the TOC/TN documents a mixed origin for the TOC that is dominated by terrestrial C3 plant organic carbon and soil organic carbon (Fig. 15). The composition of TOC at GC 955 is similar to that determined from cores in the Mississippi Canyon and Orca Basin (DSDP Leg 96) and Mars Ridge-Ursa Basin (IODP Exp. 308) (Fig. 15). The influence of marine-derived organic carbon appears to be low, consistent with the low abundance of *in situ* microfossils in the reservoir sediments.

The $CaCO_3$ content throughout the reservoir is significant, with a mean of 14.29 wt% ($1\sigma = 3.06$) and a range of 7.32 to 21.22 wt%. These amounts and presence are consistent with the detrital carbonate lithic fragments (Fig. 5) and the reworked Cretaceous calcareous nannofossils (Fig. 7) observed in smear slides. The range in $CaCO_3$ wt% is also consistent with the XRD observation of calcite (5.9 to 11.7 wt%), dolomite (8.4 to 10.7 wt%), and siderite (0.2 to 0.9 wt%) in H005 samples (15.8 to 20.9 total carbonate wt%) (Meazell et al., 2020). The predominance of the consistent, enriched signature of the δ^{13}C-TC in the total carbon measurements (TC = TOC + $CaCO_3$) reflects the significant fraction of $CaCO_3$ throughout the reservoir sediments (Fig. 13).

5.7.2. TS and $\delta^{34}S$ isotopes

In order to track the abundance of solid phase diagenetic sulfide minerals throughout the reservoir, bulk sediment total sulfur and sulfur isotopic measurements were completed (Fig. 16A and B). In marine sediments, both organoclastic sulfate reduction (OSR) and anaerobic oxidation of methane (AOM) produce hydrogen sulfide, which in the presence of reactive iron, can precipitate pyrite, greigite, and iron monosulfide minerals (Riedinger et al., 2005; Larrasoaña et al., 2007; Johnson et al., 2021). Near the SMTZ, elemental sulfur and organic sulfur can also be precipitated (Riedinger et al., 2017).

As observed in modern seafloor methane-seep environments and at SMTZs (e.g., Kaneko et al., 2010; Sato et al., 2012), measurements of TS are elevated relative to that expected to be produced by OSR (Berner and Raiswell, 1983). This excess TS is driven by methane transported toward the SMTZ, where it is consumed during AOM. In the GC 955 reservoir we observed excess TS relative to TOC that is consistent with the occurrence of early, AOM related, diagenesis in the reservoir sediments (Fig. 16C). Throughout the GC 955 reservoir, we observe two intervals of enhanced TS: between 410 and 424 mbsf and 437–446.5 mbsf, near the top and bottom of the reservoir (Fig. 16). These intervals of elevated TS (up to 2 wt%) relative to the background level (~0.2 wt%) throughout the reservoir, correspond to enriched (positive) bulk sediment δ^{34}S-TS measurements, which are a good proxy for chromium reducible sulfur in methane seep environments (Turner, 2018) and are diagnostic of sulfides produced via AOM (e.g. Peketi et al., 2012; Borowski et al., 2013). These two intervals indicate that AOM was a dominant process within the reservoir sediments and resulted in isotopically enriched sulfide mineral precipitation. This AOM diagenetic overprint occurred in the presence of pore water sulfate and methane and thus occurred during early diagenesis, prior to compaction/dewatering.

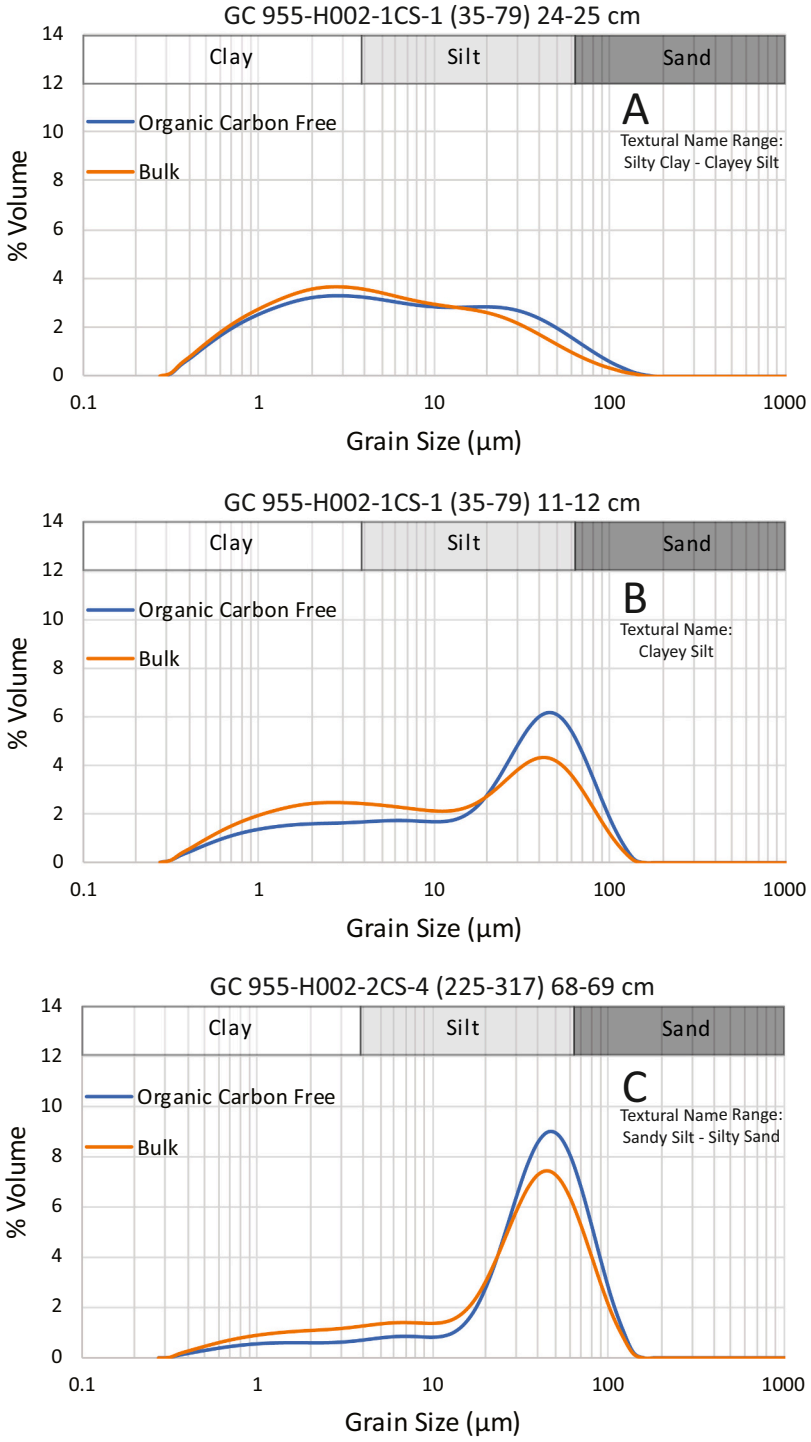

Fig. 12. Example bulk sediment and organic carbon-free sediment replicate measurements for each grain size distribution type. Portions of the plots where the organic carbon-free fraction is less than the bulk indicate the size fraction where organic carbon resides in each sample. A relative coarsening of the sample is apparent after the removal of the organic carbon. (For interpretation of the references to color in this figure, the reader is referred to the web version of this article.)

6. Discussion

6.1. Depositional history and sediment provenance

Turbidity currents and other submarine sediment gravity flows transport coarse sediments from the continental shelf out to the abyssal plain, where hemipelagic sedimentation is typically dominated by clay and silt-sized lithogenic (mineral and rock fragments) and biogenic (fecal pellets and microfossils) particles settling out of the water column. In this paper, the samples analyzed were collected from a Pleistocene-age channel-levee system near the mouth of Green Canyon in the Gulf of Mexico (Flemings et al., 2020; Santra et al., 2020). Age control was determined by identification of marker species of *in situ* calcareous nannofossils in the finest stratigraphic intervals (Fig. 6).

The methane hydrate-bearing reservoir at the core sites is bounded above and below by homogeneous clay-dominated sediments lacking notable flow structures (Meazell et al., 2020). Above the reservoir, the lithofacies were similar to those observed within the reservoir-

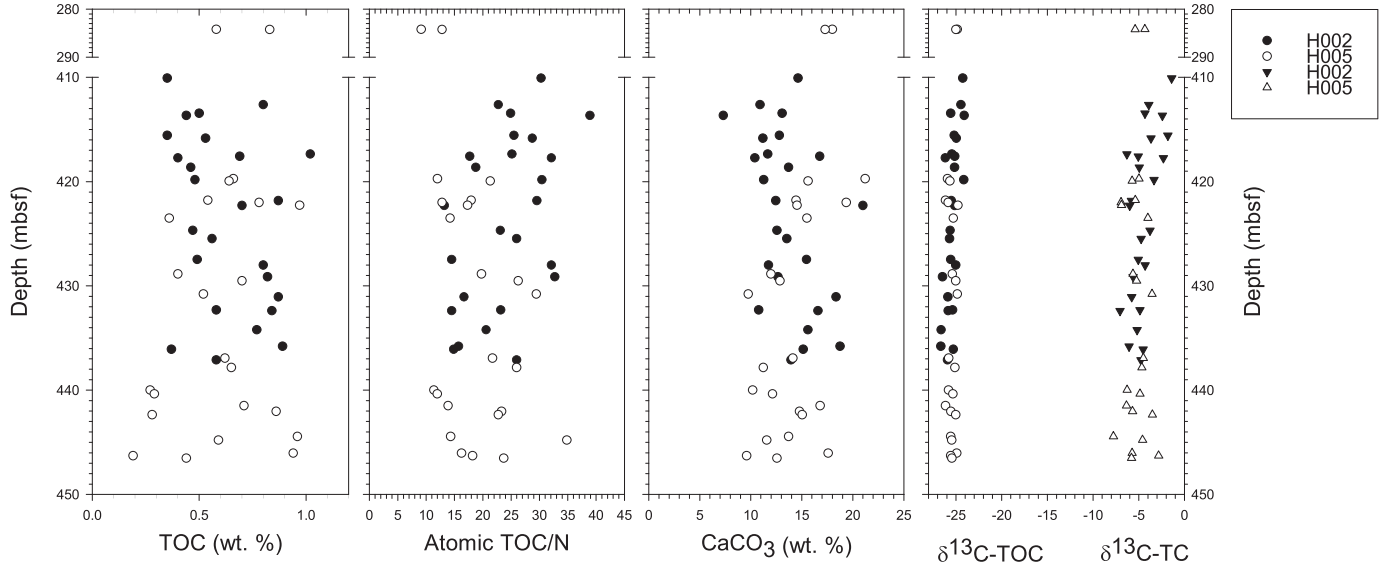

Fig. 13. Stratigraphic variations in TOC, TOC/N, $CaCO_3$, δ^{13}C-TOC, and δ^{13}C-TC, throughout the GC 955 reservoir.

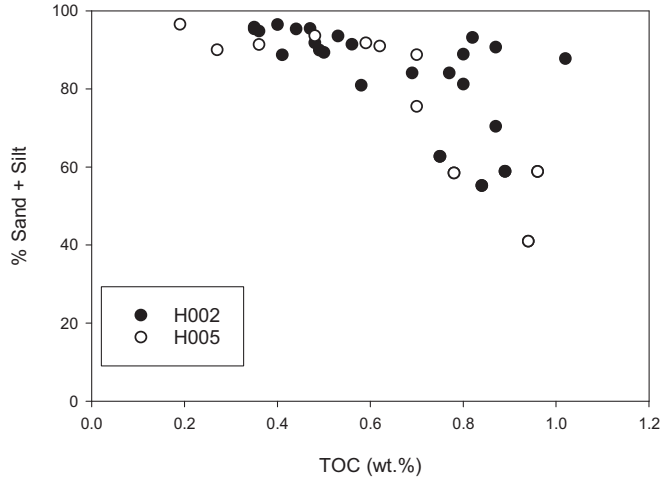

Fig. 14. The percent sand and silt grain size vs TOC for the 35 samples that were measured for both TOC and grain size.

interbedded sandy silt and clayey silt, however with notably less coarse fraction (Flemings et al., 2020). In contrast, the methane hydrate-bearing reservoir interval contains sandy silt and silty sand (C-type lithofacies) that display ripple-scale, cross laminations (Meazell et al., 2020), and are consistent with lateral sediment transport via turbidity currents that have overspilled an adjacent channel and been deposited in a levee environment. These coarser-grained sediments contain high saturations (>80%) of methane hydrate (Phillips et al., 2020). Intervals of silty clay and clayey silt (A and B-type lithofacies) are interbedded with the coarser grained reservoir lithofacies (Johnson and Divins, 2020) and many of the clay rich intervals contain thin beds and laminations of coarser grained material (e.g. Phillips et al., 2020). The levee depositional system is imaged in detail in seismic reflection data across the UT-GOM2-1 GC 955 holes and constrained by well logs, revealing extensional faults related to gravitational collapse of the levee through time (Santra et al., 2020). This levee collapse was likely due to a distinct period of high sedimentation during sustained turbidity current activity that overspilled channel confinement.

Examination of the silt and sand size sediment composition throughout the reservoir interval via smear slide petrography reveals both textural and compositional immaturity documented by an abundance of subangular to angular grains (Flemings et al., 2018; Meazell et al., 2020) and the presence of multiple feldspars and lithic fragments (Fig. 5A), including chemically and physically weak detrital carbonate and igneous grains (Fig. 5B). Sediments with a relatively immature bulk composition are also observed across the Gulf of Mexico slope and within its source rivers, the Mississippi and Rio Grande (Fig. 5A). The samples we observed from GC 955 are among the most lithic- and feldspar-rich sediment samples collected by scientific ocean drilling in the Gulf of Mexico. The immature nature of the coarse fraction (>silt) is consistent with rapid deposition of river-fed, shelf-sourced turbidity currents that dominated the slope/rise depositional environment recorded in the GC 955 cores.

The stratigraphy of the GC 995 methane hydrate reservoir alternates between finer (A-type grain size distributions) and a coarser lithofacies (C-type grain size distributions), which suggests episodic, coarse sedimentation interrupted by finer background hemipelagic sedimentation and/or stacked turbidite deposits that lack hemipelagic interbeds, which is consistent with sediment cores collected from other turbidite channel-levee systems (e.g., Riedel et al., 2010; Collett et al., 2014). The abundance of silt throughout the GC 955 reservoir implies a relatively high sedimentation rate, where the channel spilling turbidity currents had either enough velocity during transport to erode away inter-event hemipelagic sediments or were frequent enough to inhibit inter-event hemipelagic sedimentation. The lack of any obvious erosional contacts within the cores suggests high frequency events inhibited inter-event hemipelagic sedimentation and the clay-rich intervals preserved within the reservoir are likely genetically associated with turbidity currents. The B-type grain size distributions represent a hybrid between A and C-type, that most likely reflects waning turbidity current energy, just prior to the start of a hemipelagic regime. The limited presence of Pleistocene calcareous nannofossils throughout the reservoir (Figs. 6 and 7) and their restricted abundance to the fine-grained sediments attests to the lack of well-preserved hemipelagic intervals. In addition, the predominance of reworked Cretaceous calcareous nannofossils (Fig. 7) and detrital carbonate lithic grains (Fig. 5B) reflects primarily turbidity current deposition and reworking of the reservoir sediments. The result is a stacked turbidite levee sequence that although contains a clay fraction within each event deposit (e.g. Fig. 8), is dominated by the coarser turbidite beds, a conclusion consistent with the conceptual depositional model of Meazell et al. (2020).

The textural classification of the type B lithofacies is clayey-silt

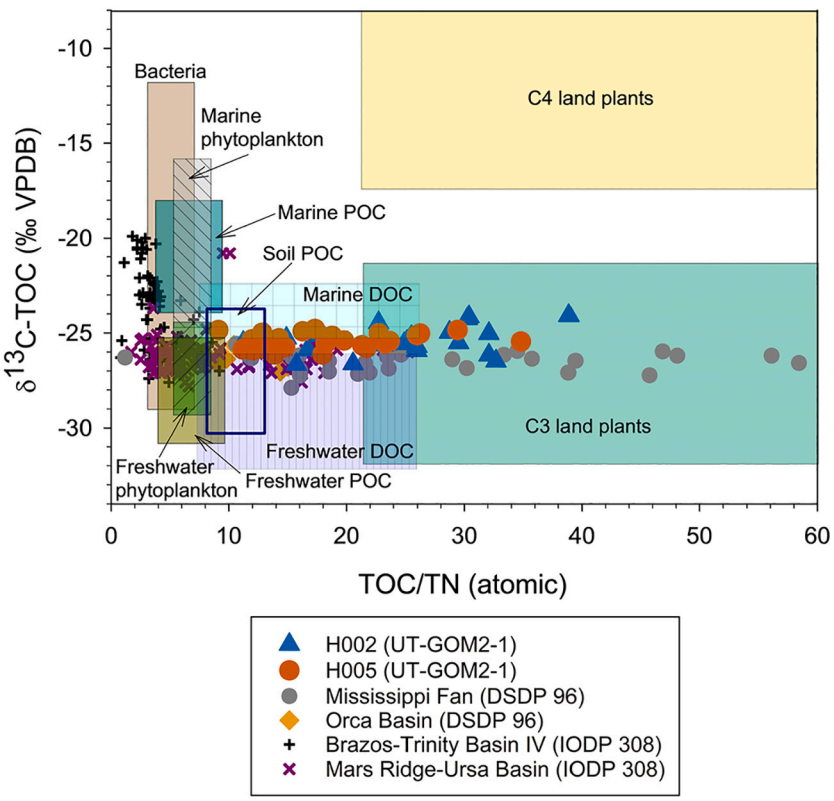

Fig. 15. Atomic TOC/TN versus isotopic δ^{13}C-TOC ratios of sediments for holes H002 and H005 along with data from the Mississippi Fan (Deep Sea Drilling Project, DSDP Sites 614-617, 620-624) (Kennicutt II et al., 1986), Orca Basin (DSDP Sites 618–619) (Kennicutt II et al., 1986), Brazos-Trinity Basin IV (Integrated Ocean Drilling Program, IODP Sites U1319-U1320) (Gilhooly III et al., 2008), and Ursa Basin (IODP Sites U1322, U1324) (Gilhooly III et al., 2008). Fields for carbon sources are based on Mayer (1994), Lamb et al. (2006), and Goni et al. (2008). (For interpretation of the references to color in this figure legend, the reader is referred to the web version of this article.)

(Fig. 9), consistent with the clayey silt of Meazell et al. (2020). This lithofacies was not easily identified during initial core description and smear slide analysis, instead it was revealed in our grain size data due to its distinct bimodal grain size distribution and a median grain size between that of the Type A and C lithofacies. We interpret the Type B lithofacies to represent sediment deposition at the distal margin of waning turbidity currents, where turbidity and/or flow velocity ceases and the remaining suspended sediment begins to settle out of the water column. As turbidity current energy wanes and then finally ceases, the remaining suspended grains are deposited together. Sediment deposition in the waning stages of turbidity current energy is therefore the least sorted turbidite-related lithofacies, consistent with our measured sorting (Fig. 11). The Type B lithofacies is differentiated from the Type C lithofacies because it represents the final stages of turbidity-current deposition, where silt and clay are deposited together due to a rapid reduction in depositional energy. The deposition of Type B and C lithofacies throughout the reservoir is likely controlled by differences in the depostional energy and/or proximity of individual turbidity-current events to the levee.

Coarsest 1% of sediments vs. median grain size plots (CM plots) were first introduced by Passega (1957) and later modified by Passega (1964), Passega and Byramjee (1969), and Ludwikowska-Kędzia (2000). The CM plot (Fig. 17) was initially created by observing modes of sediment transport in rivers, and later used to analyze turbidites (e.g., Passega, 1957, 1964). The value of the CM plot is in its ability to illustrate the processes of sediment transport and deposition. Holes H002 and H005 are located on a levee above a Pleistocene-age sediment channel so sedimentation at this location is driven by suspended sediments escaping the main sediment channel during turbidity current events and any interevent sedimentation. Fine sediments are more easily suspended than coarse, so the fields outlining transport by suspension on Fig. 17 have lower median grain sizes and their coarsest sediment grains are also smaller. Sediment grains small enough to be transported, but larger than can be continually suspended are transported by bedload processes. As expected, beach deposits are dominated by bedload transport and fluvial deposits reflect both bedload and suspension transport (Fig. 17). Coarse grain turbidity currents lie parallel and near to the 1:1 between the coarsest 1% and median grain sizes (Passega, 1964; Fig. 17).

The silt dominated turbidite levee deposits at GC 955 define a new regime on the CM plot, dominated by suspension and extending across a wide distribution of grain sizes (Fig. 17). The distribution of GC 955 sediments (Fig. 17, shaded in grey) reflects the deposition of silt dominated turbidity currents that grade in grain size during the wanning stages of turbidity current energy in this overbank, levee depositional environment. The pelagic suspension depositional regime defined by Passega (1964) overlaps with the GC 955 data, suggesting the wanning energy regime of turbidity currents is difficult to decipher from sedimentation driven by pelagic settling. We note however, the low abundance of microscopic phytoplankton and zooplankton microfossils in the GC 955 sediments, as well as the limited preservations of *in situ* (Pleistocene) calcareous nannofossils, suggests true pelagic or hemipelagic interevent sedimentation was not preserved, leaving the reservoir a sequence of stacked, silt-dominated, levee turbidites (e.g. Van Daele et al., 2017). We suggest that true hemipelagic or pelagic suspension cannot be solely defined based on the GC 955 grain size distribution, but instead, the presence/absence, identification, and size fraction of the biogenic fraction must be considered. To account for this, we add an arrow to Fig. 17 identifying the likely effect of "Increasing Biogenic Fraction" above the pelagic suspension regime of Passega (1964). In the GC 955 data set, we expect that true hemipelagic or pelagic sediments would have plotted above the silt dominated turbidity current regime defined here by the GC 955 samples (light grey triangle) to account for the presence of phyto- and zooplankton remains (foraminifers, diatoms, radiolarians), which are often much larger than the fine silt to clay sized sediments that they are deposited with (e.g. Rowe, 2017). In the GC 955 sediments, the lack of this larger biogenic fraction, amidst their presence in the Pleistocene Gulf of Mexico water column, suggests interevent sedimentation was not preserved between turbidity currents. Future particle size measurements of fine-grained marine sediments containing a biogenic fraction could test our assertion.

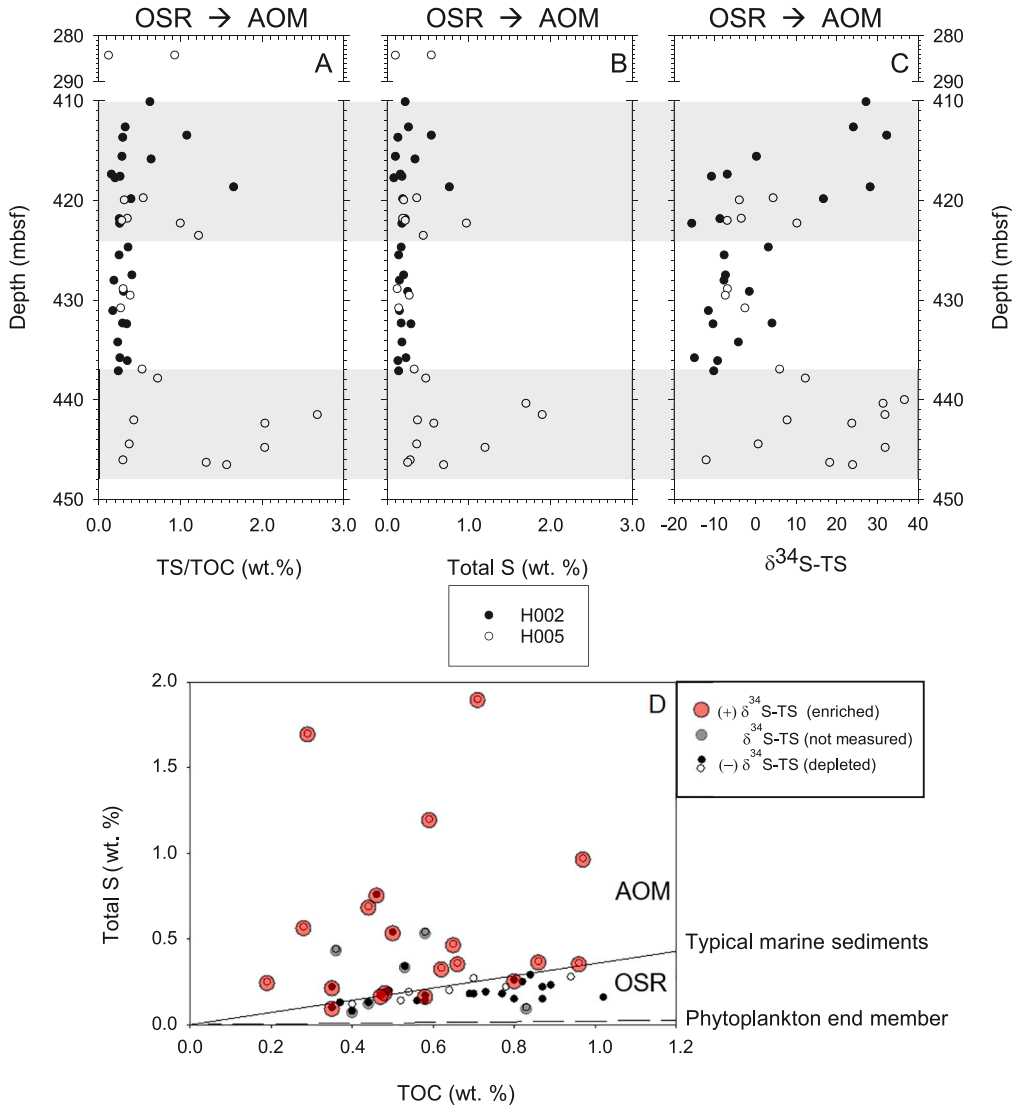

Fig. 16. (A) Bulk sediment TS/TOC, (B) Bulk sediment TS and (C) δ^{34}S-TS versus depth throughout the UT-GOM2-1 reservoir. (D) TS versus TOC data document elevated TS values consistent with AOM. Enriched (+) S isotopic values (red) and depleted (−) isotopic values (black and white) also differentiate AOM vs OSR diagenesis. Collectively, these data document AOM-related diagenesis in two intervals within the reservoir (grey shaded in A-C) and indicate the presence of methane in the reservoir sediments during early diagenesis. Typical marine sediments line (D) from Berner and Raiswell (1983) and marine phytoplankton base line (D) from Suits and Arthur (2000). (For interpretation of the references to color in this figure legend, the reader is referred to the web version of this article.)

6.2. *Sorting out the carbon: grainsize distributions, TOC and detrital $CaCO_3$*

Comparison of our measurements of grain size on the bulk sediment and organic carbon-free fraction from the same sample reveals organic carbon was observed in all three lithofacies (A, B, and C, Fig. 13) and predominantly in their finest fractions (Fig. 12). A notable shift in grain size distribution toward the coarser fraction, following TOC removal, was observed in 28 of 46 samples. The remaining 18 samples showed no, or only a very minor change in their grain size distribution following TOC removal. Samples showing no change in grain size distribution following organic carbon removal are not unique to any of the three identified lithofacies (A, B, or C). Based on the grain size difference plots, these 18 samples appear to contain very low organic carbon. In marine deepwater depositional settings, the organic carbon content of fine-grained sediments is typically greater than that of coarse-grained sediments, in part because organic carbon is adsorbed onto fine-grained mineral surfaces, that can sink out, protecting it from microbial regeneration in the water column (Mayer, 1994). This results in greater preservation of organic carbon in fine-grained marine sediments. Coarse-grained sediments can contain organic carbon, but it is typically particulate organic carbon of terrestrial origin that was transported and eventually deposited as larger particles with the rest of the coarse sediment load during high energy transport (Burdige, 2007). Similarly, at GC 955, TOC is higher in sediments with higher clay content (Fig. 14). It is apparent in our GC 955 data set that organic carbon, when present, is predominantly fine-grained and it is sorted and deposited with the fine fraction of the turbidite levee deposits.

In addition to inferring the presence of organic carbon based on the change in grain size after dissolution of the organic carbon by hydrogen peroxide treatments, we also measured the TOC directly (Fig. 13). The presence of a significant amount of detrital carbonate grains makes measurements of TOC in marine sediments difficult, but reliable and reproducible measurements can be achieved (Phillips et al., 2011). Comparison of the measured TOC and the grain size on 35 companion samples documents the higher TOC in the finer grained samples (Fig. 14), consistent with our bulk and organic carbon free grain size results (Fig. 12) and discussed in Section 6.5.

6.3. *AOM and OSR diagenesis and sedimentation rates*

In the bulk sediments throughout the reservoir we observe two intervals with increased TS, elevated TS:TOC, and enriched δ^{34}S-TS (Fig. 16) that correspond to enhanced zones of AOM-driven pyritization (e.g. Kaneko et al., 2010; Johnson et al., 2021) and prolonged paleopositions of the SMTZ. These enhanced diagenetic zones are

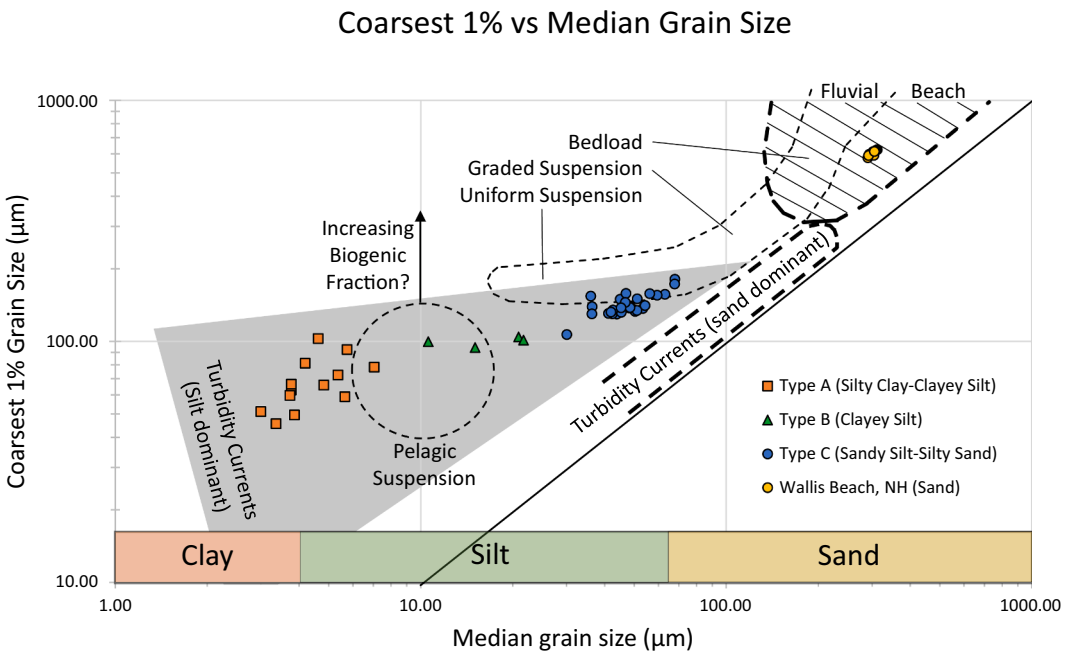

Fig. 17. CM plot showing the depositional regimes associated with beach, fluvial, and turbidity current sediment transport (modified from Tucker (1988) based on Passega (1964). Silt-dominated turbidity currents (grey shaded triangle) are defined by the GC 955 grain size data and are shown for all the measured bulk sediment Type A, B, and C grain size distributions, as well for our Wallis Beach Sand lab standard, all other fields are from Passega (1964). (For interpretation of the references to color in this figure legend, the reader is referred to the web version of this article.)

juxtaposed against a background level of low TS, low TS/TOC, and depleted $\delta^{34}S$, which is characteristic of pyritization driven by OSR (Fig. 16). Our data document paleo-preservation of early diagenetic effects in the reservoir that require labile organic carbon and sulfate (OSR) and/or methane and sulfate (AOM) availability during and shortly after (pre-compaction and dewatering) deposition of the sediments.

The products of these diagenetic reactions include iron sulfide minerals, dominated by pyrite, and authigenic carbonates. Although authigenic carbonates are not observed in the cores, beyond trace amounts in smear slide, some pyrite and/or possibly other iron sulfides are clearly present in the sediment. In other methane hydrate-bearing or methane seep continental margin environments, these diagenetic precipitates can overwhelm the sediment records, eliminating primary porosity (e.g. Greinert et al., 2001), while in others they can help preserve primary porosity (e.g. Rose et al., 2014). In the GC 955 record, these early diagenetic precipitates appear to be limited to iron sulfide precipitation that was enhanced in two zones within the reservoir (Fig. 16), but was not sufficient to inhibit the primary porosity that was later filled with the high methane hydrate saturations currently observed throughout the reservoir (Phillips et al., 2020). The mobility of methane in the sediments, which can be generated *in situ* or supplied from deeper sediments, relative to TOC, along with relative decrease in sedimentation rate to stall the SMTZ may have helped enhance early AOM-driven pyritization.

In contrast, OSR-driven pyritization may have been limited by the type and fixed amount of *in situ* TOC in the sediments. In effect, the enhanced zones of increased TS provide us with a possible indicator of relative changes in sedimentation rate within the silt-rich GC 955 reservoir, that are otherwise not apparent in our grain size, core descriptions, or biostratigraphic data. Slower sedimentation rates allow for more time for H_2S to be produced via AOM and to react with iron, resulting in higher abundances of pyrite and higher TS. In this case the sedimentation rate would have been slower during the early deposition of the channel-levee, increasing through the middle stage, and followed by a decrease in the final stages of levee sedimentation. These changes in sedimentation rate were likely driven by less frequent and/or less energetic turbidity current activity in the adjacent channel, which had a notable effect on the sediment deposition and early diagenesis at our GC 955 sites. Although we see some evidence that the SMTZ persisted in time and enhanced AOM induced pyritization, more generally, the stacked turbidites deposited in the levee environment represent a high sedimentation rate environment. In this scenario, these rapid sedimentation events may actually inhibit diagenetic porosity losses due to OSR and AOM diagenetic precipitates, by allowing the sediments to rapidly pass through the SMTZ, thus keeping the coarse reservoir open for later methane hydrate formation.

6.4. TOC distribution and methanogenesis

Methane stored in the methane hydrate reservoir at GC 955 is produced by the microbial degradation of organic carbon (Moore et al., 2020, 2022; Phillips et al., 2020). In the marine environment, methanogenesis occurs under anoxic porewater conditions beneath the seafloor, in stratigraphy containing sufficient buried organic carbon to deplete pore water sulfate. Methane hydrate saturation in marine reservoirs ranges from a few percent to nearly 100% saturation of available pore space, with the coarser, sand-rich stratigraphy containing the greatest saturations (e.g., Torres et al., 2008; Ito et al., 2015; Collett et al., 2019; Phillips et al., 2020). In marine deepwater depositional settings, the organic carbon content of fine-grained sediments is typically greater than that of coarse-grained sediments, resulting in greater preservation of organic carbon in fine-grained marine sediments. Coarse-grained sediments generally contain lower organic carbon and typically particulate organic carbon of terrestrial origin that was transported during high energy conditions.

If methane hydrate saturations are higher in coarse-grained stratigraphic intervals, methane formed in finer-grained stratigraphic intervals likely migrated via diffusion and/or advection into the coarse-grained reservoirs (Wei et al., 2019). Short-range methane migration (<10's of meters) occurs when methane is produced in one stratigraphic section and migrates to an adjacent stratigraphic section, by means of

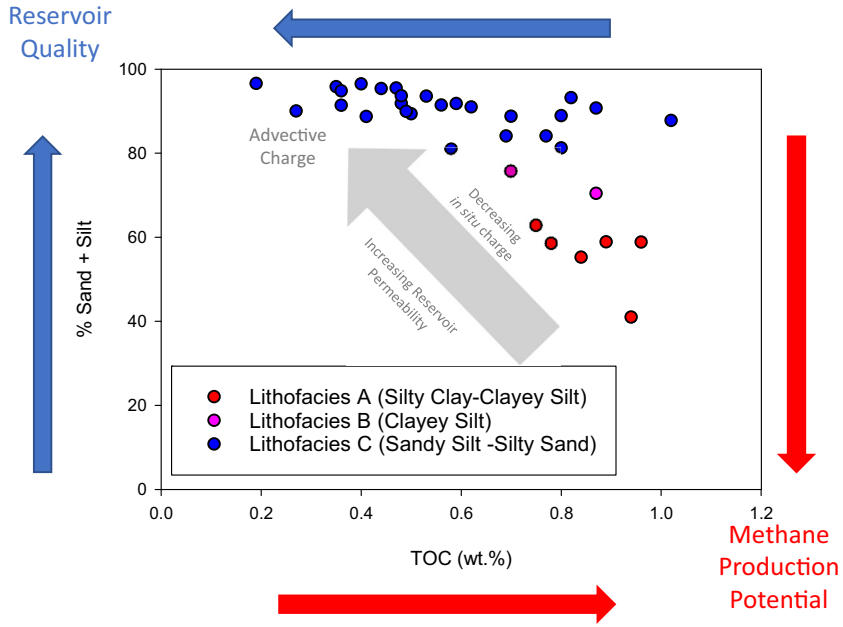

Fig. 18. The percent sand and silt grain size vs TOC for 35 samples that were measured for both TOC and grain size throughout the UT-GOM2-1 reservoir (from Fig. 14) plotted here by lithofacies type (A, B, and C). Annotations and implications for *in situ* versus *ex situ* methane charge are discussed in the text. (For interpretation of the references to color in this figure legend, the reader is referred to the web version of this article.)

diffusion or advection, where it can subsequently form methane hydrate (Malinverno, 2010; Cook et al., 2014). In this case, dissolved methane produced in fine stratigraphic intervals, where pore spaces are very small, can migrate into nearby coarse intervals, which offers larger pore spaces, and subsequently form methane hydrate when methane solubility is exceeded (Malinverno, 2010; Liu and Flemings, 2011).

Long-range methane migration occurs when methane is produced in one place and migrates, by means of diffusion or advection, a long distance (>10's of meters) before forming methane hydrate. Methane can migrate great distances given sufficient permeable pathways, such as along coarse turbidite beds that have been tilted or through faults and fractures. The core sites at GC 955 are underlain by a salt diapir that has deformed and fractured the overlying stratigraphy (McConnell, 2000; Heggland, 2004; Portnov et al., 2019), including the methane hydrate reservoir discussed in this paper. Seismic imaging of strata overlying the salt diapir at GC 955 identify the methane hydrate reservoir encountered while drilling holes H002 and H005, as well as deeper seismic anomalies that could be relict reservoirs and/or sources of methane gas (Portnov et al., 2019). Several faults extend vertically through the gas-hydrate reservoir and could act as highly permeability conduits for long-range methane migration of deeper gas to the main methane hydrate reservoir. The presence of the methane hydrate reservoir relative to several deeper seismic anomalies connected with faults, suggests that long-range methane migration from deeper stratigraphy may be the main charge mechanism for the UT-GOM2-1 methane hydrate reservoir.

Methanogenesis supplying methane to the methane hydrate reservoir at GC 955 may be occurring within fine-grained stratigraphy nearby the reservoir (short-range migration), in stratigraphy far from the methane hydrate reservoir (long-range migration), or *in situ*. Short-range methane migration is likely contributing to methane transport and accumulation in the methane hydrate reservoir given the presence of elevated organic carbon content measured in the fine-grained stratigraphy of the reservoir (Figs. 13 and 14). Short-range migration models suggests that methanogenesis in fine-grained sediments with organic carbon content as low as 0.2 wt% can supply enough methane for high saturations of methane hydrate in relatively thin (~3 m or less) coarse-grained beds, but not within thick sand sequences (You and Flemings, 2018; You et al., 2019; Wei et al., 2019). Numerical simulations by Wei et al. (2021) specifically focused on the dimensions and properties of the GC 955 reservoir suggest that although some methane may be produced locally, free gas flow is necessary to attain the extreme hydrate saturations (up to 93%) observed in this reservoir (Phillips et al., 2020). These models further support the geological framework for long-range methane migration at GC 955.

6.5. *Implications of grainsize and TOC on gas charge*

Using the binned GC 955 grain size and TOC cross plot we can infer much about the expected history and behavior of this and other methane hydrate reservoirs in the marine environment (Fig. 18). The GC 955 data clearly show the highest TOC bearing sediments are in the finer grained sediments of the reservoir, which accordingly offer the highest methane production potential. Though the coarsest sediments of the reservoir contain the least amount of TOC, they offer primary porosity that drives high reservoir quality. Reservoir sediments that plot toward the upper left corner of Fig. 18 are most likely to offer high porosity and permeability (Fang et al., 2020, 2022), but their low TOC content makes them less prone to *in situ* methanogenesis, instead requiring advective delivery of methane from elsewhere to provide methane for free gas or methane hydrate formation. Conversely, reservoirs characterized by sediments that plot in the lower right corner of Fig. 17, are more likely to be sources for methanogenesis that could charge a reservoir *in situ* or via short range migration. As the GC 955 reservoir extends across entire Fig. 18 plot, including a measurable component of high sand + silt % with high TOC in the upper right quadrant (lithofacies C), some *in situ* methanogenesis and short-range migration of methane is possible, however, long range migration of gas most likely explains the high methane hydrate saturations currently observed in the reservoir.

7. Conclusions

In this study we use sedimentology and sediment geochemistry to characterize a silt dominated methane hydrate reservoir in the Gulf of Mexico. We present several data sets: sediment composition, biostratigraphic age, grain size, TOC, C/N, δ^{13}C-TOC, $CaCO_3$, TS, and δ^{34}S-TS from sediments collected with pressure cores from a methane hydrate

rich, turbidite channel-levee system during the 2017 UT-GOM2-1 Hydrate Pressure Coring Expedition. Collectively, these measurements characterize the depositional and diagenetic processes that influenced the accumulation of significant methane hydrate throughout the reservoir. Our results indicate the reservoir is composed of three distinct lithofacies that are characteristic of variable turbidity current energy regimes within the Pleistocene channel-levee environment. We also document that the TOC in the sediments of the reservoir is sorted in the fine fraction of each lithofacies, while the $CaCO_3$ (biogenic) fraction is reworked and part of the detrital load. The rapid progression of these sediments through the SMTZ restricted OSR and AOM related mineralization to iron sulfides, which occurred in greatest abundance in two zones within the reservoir. The two zones of iron sulfide diagenesis were both likely produced during stalled SMTZ positions driven by relative decreases in sedimentation rate. The low level of diagenetic precipitates throughout the reservoir allowed the primary porosity to remain largely intact and subsequently filled with high saturation pore-filling methane hydrate. TOC within the reservoir is likely to have resulted in some methanogenesis, however the high methane hydrate saturations observed here most likely required advection of gas from deeper sediments, transported along faults that traverse the GHSZ. The results presented in this research, coupled with recovered methane hydrate in the pressure cores, suggest that rapidly deposited, silt-dominated channel-levee environments may inhibit significant early diagenetic mineralization, thus preserving primary porosity for subsequent accumulation of methane hydrate through time and have important implications for the distribution of methane hydrate in marine sediments along continental margins.

Disclaimer

Any use of trade, firm, or product names is for descriptive purposes only and does not imply endorsement by the U.S. Government. This report was prepared as an account of work sponsored by the United States Government. Neither the U.S. Department of Energy nor any of their employees make any warranty, express or implied or assume any legal liability or responsibility for the accuracy, completeness, or usefulness of any information, apparatus, product, or process disclosed, or represent that its use would not infringe on privately owned rights. This paper has been peer reviewed and approved for publication consistent with U.S. Geological Survey Fundamental Science Practices (https://pubs.usgs.gov/circ/1367/). The views and opinions expressed within this paper represent those of the authors and the U.S. Geological Survey, but not the U.S. Department of Energy.

Data availability

The complete sediment core logs and grain size data are permanently archived and available on the UT-GOM2-1 expedition website. They are referenced throughout the paper as Johnson and Divins, 2020 and Johnson et al., 2020. The geochemical data ($CaCO_3$,TOC, C/N, $\delta^{13}C$, TS, $\delta^{34}S$) is available as Supplementary Data Table S1.

Declaration of Competing Interest

The authors declare that they have no known competing financial interests or personal relationships that could have appeared to influence the work reported in this paper.

Acknowledgements

This research and the UT-GOM2-1Hydrate Pressure Coring Expedition was supported by the U.S. Department of Energy (DOE) through Project # DE-FE0023919 “Deepwater Methane Hydrate Characterization and Scientific Assessment”. Graduate Teaching Assistant support and additional research funds for co-author MacLeod were provided through the UNH Dept. of Earth Sciences and the Jonathan W. Herndon Scholarship. Co-author Phillips was supported by funding from the U.S. Geological Survey’s Coastal and Marine Hazards and Resources Program and DOE Interagency Agreement89243320SFE000013. We gratefully acknowledge Matthew Frye (BOEM) and Cecilia McHugh (Queens College, CUNY) for their constructive reviews. We also acknowledge William Waite (USGS) for his constructive USGS internal review.

Appendix A. Supplementary data

Supplementary data to this article can be found online at https://doi.org/10.1016/j.margeo.2021.106718.

References

Amery, G.B., 1969. Structure of sigsbee scarp. AAPG Bull. 53, 2480–2482. https://doi.org/10.1306/5D25C969-16C1-11D7-8645000102C1865D.

Archer, D., Buffett, B., Brovkin, V., 2009. Ocean methane hydrates as a slow tipping point in the global carbon cycle. Proc. Natl. Acad. Sci. U. S. A. 106 (49), 20596–20601. https://doi.org/10.1073/pnas.0800885105.

Backman, J., Raffi, I., Rio, D., Fornaciari, E., Pälike, 2012. Biozonation and biochronology of Miocene through Pleistocene calcareous nannofossils from low and middle latitudes. Newsl. Stratigr. 45 (3), 221–244.

Berner, R.A., Raiswell, R., 1983. Burial of organic carbon and pyrite sulfur in sediments over Phanerozoic time: a new theory. Geochim. Cosmochim. Acta 47, 855–862. https://doi.org/10.1016/0016-7037(83)90151-5.

Borowski, W.S., Rodriguez, N.M., Paull, C.K., Ussler, W., 2013. Are ^{34}S-enriched authigenic sulfide minerals a proxy for elevated methane flux and gas hydrates in the geologic record? Mar. Pet. Geol. 43, 381–395. https://doi.org/10.1016/j.marpetgeo.2012.12.009.

Boswell, R., 2009. Is gas hydrate energy within reach? Science 325, 957–958. https://doi.org/10.1126/science.1175074.

Boswell, R., Collett, T., 2006. The Gas Hydrate Resource Pyramid, vol. 2. US Department of Energy Methane Hydrate Letter, pp. 1–4.

Boswell, R., Collett, T.S., 2011. Current perspectives on gas hydrate resources. Energy Environ. Sci. 4, 1206–1215. https://doi.org/10.1039/C0EE00203H.

Boswell, R., Collett, T.S., Frye, M., Shedd, W., McConnell, D.R., Shelander, D., 2012a. Subsurface gas hydrates in the northern Gulf of Mexico. Mar. Pet. Geol. 34 (1), 4–30. https://doi.org/10.1016/j.marpetgeo.2011.10.003.

Boswell, R., Frye, M., Shelander, D., Shedd, W., McConnell, D.R., Cook, A.E., 2012b. Architecture of gas-hydrate-bearing sands from Walker Ridge 313, Green Canyon 955, and Alaminos Canyon 21: Northern Deepwater Gulf of Mexico. Mar. Pet. Geol. 34, 134–149. https://doi.org/10.1016/j.marpetgeo.2011.08.010.

Boswell, R., Hancock, S., Yamamoto, K., Collett, T., Pratap, M., Lee, S-R., 2020. Natural gas hydrates: status of potential as an energy resource. In: Letcher, T.M. (Ed.), Future Energy, 3rd. Elsevier, pp. 111–131.

Boswell, R., Schoderbek, D., Collett, T.S., Ohtsuki, S., White, M., Anderson, B.J., 2017. The Iġnik Sikumi field experiment, Alaska North Slope: design, operations, and implications for CO2−CH4 exchange in gas hydrate reservoirs. Energy Fuel 31, 140–153. https://doi.org/10.1021/acs.energyfuels.6b01909.

Brooks, J.M., Kennicutt, M.C., Fay, R.R., McDonald, T.J., Sassen, R., 1984. Thermogenic hydrates in the Gulf of Mexico. Science 225, 409–411. https://doi.org/10.1126/science.225.4660.409.

Burdige, D.J., 2007. Preservation of organic matter in marine sediments: controls, mechanisms, and an imbalance in sediment organic carbon budgets? Chem. Rev. 107, 467–485. https://doi.org/10.1021/cr050347q.

Collett, T., Lee, M., Lewis, R., Mrozewski, S., Guerin, G., Goldberg, D., Cook, A., 2012. Gulf of Mexico gas hydrate joint industry project leg II logging-while-drilling data acquisition and analysis. Mar. Pet. Geol. 34 (1), 41–61. https://doi.org/10.1016/j.marpetgeo.2011.08.003.

Collett, T.S., Boswell, R., Cochran, J.R., Kumar, P., Lall, M., Mazumdar, A., Ramana, M. V., Ramprasad, T., Reidel, M., Sain, K., Sathe, A.V., Vishwanath, K., 2014. Geologic implications of gas hydrates in the offshore of India: results of the National gas hydrate program expedition 01. Mar. Pet. Geol. 58A, 3–28. https://doi.org/10.1016/j.marpetgeo.2014.07.021.

Collett, T.S., Boswell, R., Waite, W.F., Kumar, P., Roy, S.K., Chopra, K., Singh, S.K., Yamada, Y., Tenma, N., Pohlman, J., Zyrianova, M., the NGHP Expedition 02 Scientific Party, 2019. India national gas hydrate program expedition 02 summary of scientific results: gas hydrate systems along the eastern continental margin of India. Mar. Pet. Geol. 108, 39–142. https://doi.org/10.1016/j.marpetgeo.2019.05.023.

Constans, R.E., Parker, M.E., 1986. Calcareous nannofossil biostratigraphy and paleoclimatic indices for the late Quaternary, Deep Sea Drilling Project, Leg 96. In: Gulf of Mexico, Initial Reports of the Deep Sea Drilling Project, 96, pp. 601–630. https://doi.org/10.2973/dsdp.proc.96.132.1986.

Cook, A.E., Goldberg, D., 2008. Extent of gas hydrate filled fracture planes: implications for *in situ* methanogenesis and resource potential. Geophys. Res. Lett. 35, L15302. https://doi.org/10.1029/2008GL034587.

Cook, A.E., Goldberg, D.S., Malinverno, A., 2014. Natural gas hydrates occupying fractures: a focus on non-vent sites on the Indian continental margin and the northern Gulf of Mexico. J. Mar. Pet. Geol. 58, 278–291. https://doi.org/10.1016/j.marpetgeo.2014.04.013.

Darnell, K.N., Flemings, P.B., DiCarlo, D., 2017. Subsurface injection of combustion power plant effluent as a solid-phase carbon dioxide storage strategy. Geophys. Res. Lett. 44, 5521–5530. https://doi.org/10.1002/2017GL073663.
Davidson, D.W., Garg, S.K., Gough, S.R., Handa, Y.P., Ratcliffe, C.I., Ripmeester, J.A., Tse, J.S., 1986. Laboratory analysis of a naturally occurring gas hydrate from sediment of the Gulf of Mexico. Geochim. Cosmochim. Acta 50, 619–623. https://doi.org/10.1016/0016-7037(86)90110-9.
Di Stefano, C., Ferro, V., Mirabile, S., 2010. Comparison between grain size analyses using laser diffraction and sedimentation methods. Biosyst. Eng. 106 (2), 205–215. ISSN 1537–5110. https://doi.org/10.1016/j.biosystemseng.2010.03.013.
Dickens, G.R., 2003. Rethinking the global carbon cycle with a large, dynamic and microbially mediated gas hydrate capacitor. Earth Planet. Sci. Lett. 213 (3–4), 169–183. https://doi.org/10.1016/S0012-821X(03)00325-X.
Ewing, M., Ewing, J., 1962. Rate of salt-dome growth. AAPG Bull. 46, 708–709. https://doi.org/10.1306/BC74385F-16BE-11D7-8645000102C1865D.
Fang, Y., Flemings, P.B., Daigle, H., Phillips, S.C., Meazell, P.K., You, K., 2020. Petrophysical properties of the GC 955 hydrate reservoir inferred from reconstituted sediments: implications for hydrate formation and production: American Association of Petroleum Geologist. AAPG Bull. 104 (9), 1997–2028. https://doi.org/10.1306/01062019165.
Flemings, P.B., Phillips, S.C, Collett, T., Cook, A., Boswell, R., and the UT-GOM2-1 Expedition Scientists, 2018. UT-GOM2-1 hydrate pressure coring expedition summary. In Flemings, P.B., Phillips, S.C, Collett, T., Cook, A., Boswell, R., and the UT-GOM2-1 Expedition Scientists, UT-GOM2-1 Hydrate Pressure Coring Expedition Report: Austin, TX (University of Texas Institute for Geophysics, TX). https://doi.org/10.2172/1647223.
Fang, Y., Flemings, P.B., Daigle, H., Phillips, S.C., O'Connell, J., 2022. Permeability of methane hydrate-bearing sandy silts in the Deepwater Gulf of Mexico (Green Canyon Block 955). AAPG Bull. https://doi.org/10.1306/08102121001.
Flemings, P.B., Phillips, S.C., Boswell, R., Collett, T.S., Cook, A.E., Dong, T., Frye, M., Guerin, G., Goldberg, D.S., Holland, M.E., Jang, J., Meazell, K., Morrison, J., O'Connell, J.I., Pettigrew, T., Petrou, E.G., Polito, P.J., Portnov, A., Santra, M., Schultheiss, P.J., Seol, Y., Shedd, W., Solomon, E.A., Thomas, C.M., Waite, W.F., You, K., 2020. Pressure coring a Gulf of Mexico deep-water turbidite gas hydrate reservoir: initial results from the UT-GOM2-1 hydrate pressure coring expedition. AAPG Bull. 104 (9), 1847–1876. https://doi.org/10.1306/05212019052.
Folk, R.L., Ward, W.C., 1957. Brazos River bar: a study in the significance of grain size parameters. J. Sediment. Petrol. 27, 3–26. https://doi.org/10.1306/74D70646-2B21-11D7-8648000102C1865D.
Frye, M., 2008. Preliminary evaluation of in-place gas hydrate resources: Gulf of Mexico Outer Continental Shelf: Minerals Management Service Report 2008-004. US Department of the Interior accessed February 12, 2020. https://www.boem.gov/sites/default/files/documents//MMS2008-004.pdf.
Fujii, T., Suzuki, K., Takayama, T., Tamaki, M., Komatsu, Y., Konno, Y., Yoneda, J., Yamamoto, K., Nagao, J., 2015. Geological setting and characterization of a methane hydrate reservoir distributed at the first offshore production test site on the Daini-Atsumi Knoll in the eastern Nankai Trough, Japan. Mar. Pet. Geol. 66, 310–322. https://doi.org/10.1016/j.marpetgeo.2015.02.037.
Gilhooly III, W.P., Macko, S.A., Flemings, P.B., 2008. Data report: isotope compositions of sedimentary organic carbon and total nitrogen from Brazos-Trinity Basin IV (Sites U1319 and U1320) and Ursa Basin (Sites U1322 and U1324), Deepwater Gulf of Mexico. In: Flemings, P.B., Behrmann, J.H., John, C.M., the Expedition 308 Scientists (Eds.), Proc. IODP, 308: College Station, TX (Integrated Ocean Drilling Program Management International, Inc.). https://doi.org/10.2204/iodp.proc.308.208.2008.
Goni, M.A., Monacci, N., Gisewhite, R., Crockett, J., Nittrouer, C., Ogston, A., Alin, S.R., Aalto, R., 2008. Terrigenous organic matter in sediments from the Fly River delta-clinoform system (Papua New Guinea). J. Geophys. Res. 113, F01S10. https://doi.org/10.1029/2006JF000653.
Greinert, J., Bohrmann, G., Suess, E., 2001. Gas hydrate-associated carbonates and methane venting at Hydrate Ridge: classification, distribution, and origin of authigenic lithologies. In: Paull, C.K., Dillon, W.P. (Eds.), Natural Gas Hydrates: Occurrence, Distribution, and Detection. AGU Geophys.Monogr, 124, pp. 99–113.
Haines, S., Hart, P., Collet, T., Shedd, W., Frye, M., Weimer, P., Boswell, R., 2017. High-resolution seismic characterization of the gas and gas hydrate system at Green Canyon 955, Gulf of Mexico, USA. Mar. Pet. Geol. 82, 220–237. https://doi.org/10.1016/j.marpetgeo.2017.01.029.
Heber, R., Cook, A., Sheets, J., Sawyer, D., 2020. Data report: X-ray diffraction of sediments from Green Canyon Block 955, Gulf of Mexico. In: Flemings, P.B., Phillips, S.C., Collett, T., Cook, A., Boswell, R., the UT-GOM2-1 Expedition Scientists (Eds.), Proceedings of the UT-GOM2-1 Hydrate Pressure Coring Expedition. University of Texas Institute for Geophysics, TX, Austin, TX, p. 27. https://doi.org/10.2172/1648308.
Heggland, R., 2004. Definition of geohazards in exploration 3-D seismic data using attributes and neural-network analysis. AAPG Bull. 88 (6), 857–868. https://doi.org/10.1306/02040404019.
Hillman, J.I.T., Cook, A.E., Sawyer, D.E., Küçük, H.M., Goldberg, D.S., 2017. The character and amplitude of 'discontinuous' bottom-simulating reflections in marine seismic data. Earth Planet. Sci. Lett. 459, 157–169. https://doi.org/10.1016/j.epsl.2016.10.058.
Hutchinson, D., Boswell, R., Collett, T., Dai, J.C., Dugan, O., Frye, M., Mcconnell, D., Rose, K., Shedd, W., Shelander, D., Wood, W., 2009. Gulf of Mexico Gas Hydrate Joint Industry Project Leg II: Green Canyon 955 Site Selection. Department of Energy, Washington, DC. https://netl.doe.gov/sites/default/files/netl-file/GC955SiteSelect%5B1%5D.pdf.
Ito, T., Komatsu, Y., Fujii, T., Suzuki, K., Egawa, K., Nakatsuka, Y., Konno, Y., et al., 2015. Lithological features of hydrate bearing sediments and their relationship with gas hydrate saturation in the eastern Nankai Trough, Japan. Mar. Pet. Geol. 66, 368–378. https://doi.org/10.1016/j.marpetgeo.2015.02.022.
Jackson, M.P.A., Talbot, C.J., 1986. External shapes, strain rates, and dynamics of salt structures. Geol. Soc. Am. Bull. 97, 305–323. https://doi.org/10.1130/0016-7606(1986)97<305:ESSRAD>2.0.CO;2.
Johnson, J.E., Divins, D.L., 2020. Data report: UT-GOM2-1 lithostratigraphic core description logs at site GC 955, holes H002 and H005. In: Flemings, P.B., Phillips, S.C., Collett, T., Cook, A., Boswell, R., the UT-GOM2-1 Expedition Scientists (Eds.), Proceedings of the UT-GOM2-1 Hydrate Pressure Coring Expedition. University of Texas Institute for Geophysics, TX, Austin, TX, p. 30. https://doi.org/10.2172/1823034.
Johnson, J.E., MacLeod, D.R., Divins, D.L., 2020. Data report: UT-GOM2-1 sediment grain size measurements at site GC 955, holes H002 and H005. In: Flemings, P.B., Phillips, S.C., Collett, T., Cook, A., Boswell, R., the UT-GOM2-1 Expedition Scientists (Eds.), Proceedings of the UT-GOM2-1 Hydrate Pressure Coring Expedition. University of Texas Institute for Geophysics, TX, Austin, TX, p. 87. https://doi.org/10.2172/1823030.
Johnson, J.E., Phillips, S.C., Clyde, W.C., Giosan, L., Torres, M.E., 2021. Isolating detrital and diagenetic signals in magnetic susceptibility records from methane-bearing marine sediments. Geochem. Geophys. Geosyst. 22, e2021GC009867 https://doi.org/10.1029/2021GC009867.
Kaneko, M., Shingai, H., Pohlman, J.W., Naraoka, H., 2010. Chemical and isotopic signature of bulk organic matter and hydrocarbon biomarkers within mid-slope accretionary sediments of the northern Cascadia margin gas hydrate system. Mar. Geol. 275 (1–4), 166–177. https://doi.org/10.1016/j.margeo.2010.05.010.
Kastner, M., Claypool, G., Robertson, G., 2008. Geochemical constraints on the origin of the pore fluids and gas hydrate distribution at Atwater Valley and Keathley Canyon, northern Gulf of Mexico. Mar. Pet. Geol. 25 (9), 860–872. https://doi.org/10.1016/j.marpetgeo.2008.01.022.
Kennicutt II, M.C., DeFreitas, D.A., Joyce, J.E., Brooks, J.M., 1986. Nonvolatile organic matter in sediments from sites 614 to 623, deep sea drilling project Leg 96. In: Bouma, A.H., Coleman, J.M., Meyer, A.W., et al. (Eds.), Init. Repts. DSDP. US. Govt. Printing Office, Washington, p. 96.
Koh, D.-Y., Kang, H., Lee, J.W., Park, Y., Kim, S.-J., Lee, J., Lee, J.Y., Lee, H., 2016. Energy-efficient natural gas hydrate production using gas exchange. Appl. Energy 162, 114–130. https://doi.org/10.1016/j.apenergy.2015.10.082.
Kou, W.-H., Smith, M.A., Ahmed, A., Kuzela, R., 2007. Direct seismic indicators of gas hydrates in the Walker Ridge and Green Canyon areas, Deepwater Gulf of Mexico. Lead. Edge 26, 152–155. https://doi.org/10.1190/1.2542440.
Kramer, K.V., Shedd, W.W., 2017. A 1.4-billion-pixel map of the Gulf of Mexico seafloor. Eos 98, 2017. https://doi.org/10.1029/2017EO073557. Published on 24 May.
Kvenvolden, K.A., 1993. Gas hydrates – geological perspective and global change. Rev. Geophys. 31 (2), 173–187. https://doi.org/10.1029/93RG00268.
Lamb, A.L., Wilson, G.P., Leng, M.J., 2006. A review of coastal palaeoclimate and relative sea-level reconstructions using δ13C and C/N ratios in organic material. Earth Sci. Rev. 75, 29–57. https://doi.org/10.1016/j.earscirev.2005.10.003.
Larrasoaña, J.C., Roberts, A.P., Musgrave, R.J., Gràcia, E., Piñero, E., Vega, M., Martínez-Ruiz, F., 2007. Diagenetic formation of greigite and pyrrhotite in gas hydrate marine sedimentary systems. Earth Planet. Sci. Lett. 261, 350–366. https://doi.org/10.1016/j.epsl.2007.06.032.
Lee, M.W., Collett, T.S., 2012. Pore- and fracture-filling gas hydrate reservoirs in the Gulf of Mexico Gas Hydrate Joint Industry Project Leg II Green Canyon 955 H well. Mar. Pet. Geol. 34 (1), 62–71. https://doi.org/10.1016/j.marpetgeo.2011.08.002.
Liu, X., Flemings, P.B., 2011. Capillary effects on hydrate stability in marine sediments. J. Geophys. Res. 112, B07102. https://doi.org/10.1029/2010JB008143.
Ludwikowska-Kędzia, M., 2000. Ewolucja środkowego Od- Cinka Doliny Rzeki Belnianki W późnym Glacjale I Holocenie [Evolution of the Middle Segment of the Belnianka River Valley in the Late Glacial and Holocene]. Dialog Press, Warsaw, p. 180.
MacDonald, I.R., Guinasso, N.L., Sassen, R., Brooks, J.M., Lee, L., Scott, K.T., 1994. Gas hydrate that breaches the sea floor on the continental slope of the Gulf of Mexico. Geology 22, 622–702. https://doi.org/10.1130/0091-7613(1994)022<0699:GHTBTS>2.3.CO;2.
MacLeod, D.R., 2020. Characterization of a Silty Methane-Hydrate Reservoir in the Gulf of Mexico: Analysis of Full Sediment Grain size Distributions. Master's Thesis, University of New Hampshire, p. 165. https://scholars.unh.edu/thesis/1387.
Madof, A.S., 2018. Gas hydrates in coarse-grained reservoirs interpreted from velocity pull up: Mississippi Fan, Gulf of Mexico. Geology 46, 559–562. https://doi.org/10.1130/G40031.1.
Majumdar, U., Cook, A.E., 2018. The volume of gas hydrate-bound gas in the northern Gulf of Mexico. Geochem. Geophys. Geosyst. 19, 4313–4328. https://doi.org/10.1029/2018GC007865.
Majumdar, U., Cook, A.E., Shedd, W., Frye, M., 2016. The connection between natural gas hydrate and bottom-simulating reflectors. Geophys. Res. Lett. 43, 7044–7051. https://doi.org/10.1002/2016GL069443.
Majumdar, U., Cook, A.E., Scharenberg, M., Burchwell, A., Ismail, S., Frye, M., Shedd, W., 2017. Semi-quantitative gas hydrate assessment from petroleum industry well logs in the northern Gulf of Mexico. Mar. Pet. Geol. 85, 233–241. https://doi.org/10.1016/j.marpetgeo.2017.05.009.
Malinverno, A., 2010. Marine gas hydrates in thin sand layers that soak up microbial methane. Earth Planet. Sci. Lett. 292, 399–408. https://doi.org/10.1016/j.epsl.2010.02.008.
Mambelli, S., Brooks, P.D., Sutka, R., Hughes, S., Finstad, K.M., Nelson, J.P., Dawson, T.E., 2016. High throughput method for simultaneous quantification of N, C and S stable isotopes and contents in organics and soils. Rapid Commun. Mass Spectrom. 30 (15), 1743–1753. https://doi.org/10.1002/rcm.7605.

Marchitto, T.M., Wei, K.-Y., 1995. History of Laurentide meltwater flow to the Gulf of Mexico during the last deglaciation, as revealed by reworked calcareous nannofossils. Geology 23 (9), 779–782. https://doi.org/10.1130/0091-7613(1995)023<0779:HOLMFT>2.3.CO;2.

Martini, E., 1971. Standard tertiary and quaternary calcareous nannoplankton zonation. In: Proceedings of the 2nd Planktonic Conference, Roma, 1970, pp. 739–785.

Mayer, L.M., 1994. Surface area control of organic carbon accumulation in continental shelf sediments. Geochem. Cosmochim. Acto 58 (4), 1271–1284. https://doi.org/10.1016/0016-7037(94)90381-6.

McConnell, D.R., 2000. Optimizing Deepwater well locations to reduce the risk of shallow-water-flow using high-resolution 2D and 3D seismic data. Offshore Technol. Conf. OTC 11973. https://doi.org/10.4043/11973-MS.

Meazell, P.K., Flemings, P.B., Santra, M., Johnson, J.E., 2020. Sedimentology and stratigraphy of a deep-water gas hydrate reservoir in the northern Gulf of Mexico. AAPG 104 (9), 1945–1969. https://doi.org/10.1306/05212019027.

Milkov, A.V., 2005. Molecular and stable isotope compositions of natural gas hydrates: a revised global data set and basic interpretations in the context of geological settings. Org. Geochem. 36 (5), 681–702. https://doi.org/10.1016/j.orggeochem.2005.01.010.

Milkov, A.V., Sassen, R., 2001. Estimate of gas hydrate resource, northwestern Gulf of Mexico continental slope. Mar. Geol. 179, 71–83. https://doi.org/10.1016/S0025-3227(01)00192-X.

Moore, M.T., Phillips, S.C., Cook, A.E., Darrah, T.H., 2020. Improved sampling technique to collect natural gas from hydrate-bearing pressure cores. Appl. Geochem. 122, 104773 https://doi.org/10.1016/j.apgeochem.2020.104773.

Moore, M.T., Phillips, S.C., Cook, A.E., Darrah, T.H., 2022. Integrated geochemical approach to determine the source of methane in gas hydrate from Green Canyon Block 955 in the Gulf of Mexico. AAPG Bull. https://doi.org/10.1306/05272120087.

Ogg, J., Ogg, G., Gradstein, F., 2016. A Concise Geologic Time Scale 2016. Elsevier B.V. ISBN978-0-444-63771-0.

Passega, R., 1957. Texture as characteristic of clastic deposition. Am. Assoc. Petrol. Geol. 41 (9), 1952–1984. https://doi.org/10.1306/0BDA594E-16BD-11D7-8645000102C1865D.

Passega, R., 1964. Grain size representation by CM patterns as a geological tool. J. Sediment. Petrol. 43 (4), 830–847.

Passega, R., Byramjee, R., 1969. Grain size image of clastic deposits. Sedimentology 13, 233–252. https://doi.org/10.1111/j.1365-3091.1969.tb00171.x.

Peel, F.J., Travis, C.J., Hossack, J.R., 1995. Genetic structural provinces and salt tectonics of the Cenozoic offshore U.S. Gulf of Mexico: a preliminary analysis. In: Jackson, M.P.A., Roberts, D.G., Snelson, S. (Eds.), Salt Tectonics: A Global Perspective: AAPG Memoir, vol. 65, pp. 153–175.

Peketi, A., Mazumdar, A., Joshi, R.K., Patil, D.J., Srinivas, P.L., Dayal, A.M., 2012. Tracing the Paleo sulfate-methane transition zones and H2S seepage events in marine sediments: an application of C-S-Mo systematics. Geochem. Geophys. Geosyst. 13, Q10007. https://doi.org/10.1029/2012/GC004288.

Pflaum, R.C., Brooks, J.M., Cox, H.B., Kennicutt II, M.C., Sheu, D.-D., 1986. Molecular and isotopic analysis of core gases and gas hydrates, Deep Sea Drilling Project Leg 96. Initial Rep. Deep Sea Drill. Proj. v. 96, 781–784. https://doi.org/10.2973/dsdp.proc.96.149.1986.

Phillips, S.C., Johnson, J.E., Miranda, E., Disenhof, C., 2011. Improving CHN measurement in carbonate-rich marine sediments. Limnol. Oceanogr. Methods 9, 194–203. https://doi.org/10.4319/lom.2011.9.194.

Phillips, S.C., Flemings, P.B., Holland, M.E., Schultheiss, P.J., Petrou, E.G., Waite, W.F., Jang, J., Hammon, H., 2020. High concentration methane hydrate in a silt reservoir from the Deepwater Gulf of Mexico. AAPG Bull. 104 (9), 1971–1995. https://doi.org/10.1306/01062018280.

Portnov, A., Cook, A.E., Sawyer, D.E., Yang, C., Hillman, J.I.T., Waite, W.F., 2019. Clustered BSRs: evidence for gas hydrate-bearing turbidite complexes in folded regions, example from the Perdido Fold Belt, northern Gulf of Mexico. Earth Planet. Sci. Lett. 528, 115843 https://doi.org/10.1016/j.epsl.2019.115843.

Portnov, A., Cook, A.E., Heidari, M., Sawyer, D.E., Santra, M., Nikolinakou, M., 2020a. Salt-driven evolution of a gas hydrate reservoir in Green Canyon, Gulf of Mexico. AAPG Bull. https://doi.org/10.1306/10151818125.

Portnov, A., Santra, M., Cook, A.E., Sawyer, D.E., 2020b. The Jackalope gas hydrate system in the northeastern Gulf of Mexico. Mar. Pet. Geol. 111, 261–278. https://doi.org/10.1016/j.marpetgeo.2019.08.036.

Potter, P.E., 1978. Petrology and chemistry of modern big river sands. J. Geol. 86, 423–449.

Prather, B.E., Booth, J.R., Steffens, G.S., Craig, P.A., 1998. Classification, lithologic calibration, and stratigraphic succession of seismic facies of intraslope basins, Deepwater Gulf of Mexico. AAPG Bull. 82 (5), 701–728. https://doi.org/10.1306/1D9BC5D9-172D-11D7-8645000102C1865D.

Purkey Phillips, M., 2020. Data report: UT-GOM2-1 biostratigraphy report Green Canyon Block 955, Gulf of Mexico. In: Proceedings of the UT-GOM2-1 Hydrate Pressure Coring Expedition. University of Texas Institute for Geophysics, TX, Austin, TX, p. 15. https://doi.org/10.2172/1823039.

Riedel, M., Collett, T.S., Malone, M., 2010. Expedition 311 synthesis: scientific findings. In: Riedel, M., Collett, T.S., Malone, M.J., the Expedition 311 Scientists (Eds.), Proc. IODP, 311. Integrated Ocean Driling Program Management International, Inc., Washington, DC https://doi.org/10.2204/iodp.proc.311.213.2010.

Riedinger, N., Pfeifer, K., Kasten, S., Garming, J.F.L., Vogt, C., Hensen, C., 2005. Diagenetic alteration of magnetic signals by anaerobic oxidation of methane related to a change in sedimentation rate. Geochim. Cosmochim. Acta 69, 4117–4126. https://doi.org/10.1016/j.gca.2005.02.004.

Riedinger, N., Brunner, B., Krastel, S., Arnold, G.L., Wehrmann, L.M., Formolo, M.J., Beck, A., Bates, S.M., Henkel, S., Kasten, S., Lyons, T.W., 2017. Sulfur cycling in an iron oxide-dominated, dynamic marine depositional system: the argentine Continental margin. Front. Earth Sci. 5, 33. https://doi.org/10.3389/feart.2017.00033.

Rose, K.K., Johnson, J.E., Torres, M.E., Hong, W.-L., Giosan, L., Solomon, E.A., et al., 2014. Anomalous porosity preservation and preferential accumulation of gas hydrate in the Andaman accretionary wedge, NGHP-01 site 17A. Mar. Pet. Geol. 58A, 99–116. https://doi.org/10.1016/j.marpetgeo.2014.04.009.

Rowe, G.T., 2017. Offshore Plankton and Benthos of the Gulf of Mexico. In: Ward, C. (Ed.), Habitats and Biota of the Gulf of Mexico: Before the Deepwater Horizon Oil Spill. Springer, New York, NY. https://doi.org/10.1007/978-1-4939-3447-8_7.

Ruppel, C., Kessler, J.D., 2017. The interaction of climate change and methane hydrates. Rev. Geophys. 55 (1), 126–168. https://doi.org/10.1002/2016RG000534.

Ruppel, C., Dickens, G.R., Castellini, D.G., Gilhooly, W., Lizarralde, D., 2005. Heat and salt inhibition of gas hydrate formation in the northern Gulf of Mexico. Geophys. Res. Lett. 32 (4), L04605, 4 p. https://doi.org/10.1029/2004GL021909.

Santra, M., Flemings, P.B., Scott, E., Meazell, K., 2020. Evolution of gas-hydrate-bearing Deepwater channel-levee system in abyssal Gulf of Mexico – levee growth and deformation. AAPG Bull. https://doi.org/10.1306/04251918177.

Sassen, R., Joye, S., Sweet, S.T., DeFeritas, D.A., Milkov, A.V., MacDonald, I.R., 1999. Thermogenic gas hydrates and hydrocarbon gases in complex chemosynthetic communities, Gulf of Mexico continental slope. Org. Geochem. 30, 485–497. https://doi.org/10.1016/S0146-6380(99)00050-9.

Sato, H., Hayashi, K., Ogawa, Y., Kawamura, K., 2012. Geochemistry of deep sea sediments at cold seep sites in the Nankai Trough: insights into the effect of anaerobic oxidation of methane. Mar. Geol. 323, 47–55. https://doi.org/10.1016/j.margeo.2012.07.013.

Shedd, W., Boswell, R., Frye, M., Godfriaux, P., Kramer, K., 2012. Occurrence and nature of “bottom simulating reflectors” in the northern Gulf of Mexico. Mar. Pet. Geol. 34 (1), 31–40. https://doi.org/10.1016/j.marpetgeo.2011.08.005.

Shipley, T.H., Houston, M.H., Buffler, R.T., Shaub, F.J., McMillen, K.J., Ladd, J.W., Worzel, J.L., 1979. Seismic evidence for widespread possible gas hydrate horizons on continental slopes and rises. AAPG Bull. 63 (12), 2204–2213.

Sperazza, M., Moore, J.N., Henrix, M.S., 2004. High-resolution particle size analysis of naturally occurring very fine-grained sediment through laser diffractometry. J. Sediment. Res. 74 (5), 736–743.

Suits, N.S., Arthur, M.A., 2000. Sulfur diagenesis and partitioning in Holocene Peru shelf and upper slope sediments. Chem. Geol. 163, 219–234. https://doi.org/10.1016/s0009-2541(99)00114-x.

Thayer, P., Roberts, H., Bouma, A., Coleman, J., 1986. Sedimentology and petrology of Mississippi Fan depositional environments. In: Deep Sea Drilling Project Leg 96. Initial reports DSDP, Leg 96, Ft. Lauderdale to Galveston, Texas, 1983, pp. 489–503. https://doi.org/10.2973/dsdp.proc.96.122.1986.

Thomas, C., Phillips, S.C., Flemings, P.B., Santra, M., Hammon, H., Collett, T.S., Cook, A. E., et al., 2020. Pressure-coring operations during the University of Texas-Gulf of Mexico 2-1 (UT-GOM2-1) hydrate pressure coring expedition in Green Canyon Block 955, northern Gulf of Mexico. AAPG Bull. 104 (9), 1877–1901. https://doi.org/10.1306/02262019036.

Torres, M.E., Tréhu, A.M., Cespedes, N., Kastner, M., Wortmann, U.G., Kim, J.-H., Long, P., Malinverno, A., Pohlman, J.W., Riedel, M., Collett, T., 2008. Methane hydrate formation in turbidite sediments of northern Cascadia, IODP Expedition 311. Earth Planet. Sci. Lett. 271 (1–4), 170–180. https://doi.org/10.1016/j.epsl.2008.03.061.

Trehu, A.M., Long, P.E., Torres, M.E., Bohrmann, G., Rack, F.R., Collett, T.S., Goldberg, D.S., Milkov, A.V., Riedel, M., Schultheiss, P., Bangs, N.L., Barr, S.R., Borowski, W.S., Claypool, G.E., Delwiche, M.E., Dickens, G.R., Gracia, E., Guerin, G., Holland, M., Johnson, J.E., Lee, Y.J., Liu, C.S., Su, X., Teichert, B., Tomaru, H., Vanneste, M., Watanabe, M., Weinberger, J.L., 2004. Three-dimensional distribution of gas hydrate beneath southern Hydrate Ridge: constraints from ODP Leg 204. Earth Planet. Sci. Lett. 222, 845–862. https://doi.org/10.1016/j.epsl.2004.03.035.

Tucker, M.E. (Ed.), 1988. Techniques in Sedimentology. Blackwell Scientific, Oxford, p. 394.

Turner, S., 2018. Tracking Sulfur Diagenesis in Methane Rich Marine Sediments on the Cascadia Margin: Comparing Sulfur Isotopes of Bulk Sediment and Chromium Reducible Sulfur (Unpublished master’s thesis). University of New Hampshire, Durham, NH, U.S.A.

Van Daele, M., Meyer, I., Moernaut, J., De Decker, S., Verschuren, D., De Batist, M., 2017. A revised classification and terminology for stacked and amalgamated turbidites in environments dominated by (hemi)pelagic sedimentation. Sediment. Geol. 357, 72–82. https://doi.org/10.1016/j.sedgeo.2017.06.007.

Waterman, A.S., Center, M.W., George, R.A., Vallette, N.S., Porter, A.F., Reilly, T.M., Roederer, R.V., Sarao, J.S., Schmieder, J., Fillon, R.H., 2017. Biostratigraphic Chart–Gulf Basin, USA: Paleogene. www.paleodata.com.

Watkins, J.S., Ladd, J.W., Buffler, R.T., Shaub, F.J., Houston, M.H., Worzel, J.L., 1978. Occurrence and evolution of salt in deep Gulf of Mexico. AAPG Stud. Geol. 7, 43–65.

Wei, L., Cook, A., Daigle, H., Malinverno, A., Nole, M., You, K., 2019. Factors controlling short-range methane migration of gas hydrate accumulations in thin coarse-grained layers. Geochem. Geophys. Geosyst. 20, 3985–4000. https://doi.org/10.1029/2019GC008405.

Wei, L., Cook, A., You, K., 2021. Methane migration mechanisms for the Green Canyon Block 955 gas hydrate reservoir, northern Gulf of Mexico. AAPG Bull. https://doi.org/10.1306/06022120134.

Wentworth, C.K., 1922. A scale of Grade and Class terms for Clastic Sediments. J. Geol. 30 (5), 377–392.

Winters, W.J., Lorenson, T.D., Paull, C.K., 2007. Initial Report of the IMAGES VIII/PAGE Gas Hydrate and Paleoclimate Cruise on the RV Marion Dufresne in the Gulf of Mexico, 2-18 July 2002, U.S. Geological Survey Open-File Report 2004-1358. http://pubs.usgs.gov/of/2004/1358/.

Worrall, D.M., Snelson, S., 1989. Evolution of the northern Gulf of Mexico, with an emphasis on Cenozoic growth faulting and the role of salt. In: Bally, A.W., Palmer, A. R. (Eds.), The Geology of North America – An Overview, A, pp. 97–138.

Xu, W., Ruppel, C., 1999. Predicting the occurrence, distribution, and evolution of methane gas hydrate in porous marine sediments from analytical models. J. Geophys. Res. 104, 5081–5096. https://doi.org/10.1029/1998JB900092.

Yamamoto, K., 2015. Overview and introduction: pressure core-sampling and analyses in the 2012–2013 MH21 offshore test of gas production from methane hydrates in the eastern Nankai Trough. Mar. Pet. Geol. 66, 296–309. https://doi.org/10.1016/j.marpetgeo.2015.02.024.

Yoneda, J., Masui, A., Konno, Y., Jin, Y., Kida, M., Katagiri, J., Nagao, J., Tenma, N., 2017. Pressure-core-based reservoir characterization for geomechanics: Insights from gas hydrate drilling during 2012-2013 at the eastern Nankai Trough. Mar. Pet. Geol. 86, 1–17. https://doi.org/10.1016/j.marpetgeo.2017.05.024.

You, K., Flemings, P.B., 2018. Methane hydrate formation in thick sand reservoirs: 1. Short-range methane diffusion. Mar. Pet. Geol. 89, 428–442. https://doi.org/10.1016/j.marpetgeo.2017.10.011.

You, K., Flemings, P.B., Malinverno, A., Collett, T.S., Darnell, K., 2019. Mechanisms of methane hydrate formation in geological systems. Rev.f Geophys. 57, 1146–1196. https://doi.org/10.1029/2018RG000638.